



Title	Meltwater Discharge From Marine-Terminating Glaciers Drives Biogeochemical Conditions in a Greenlandic Fjord
Author(s)	Kanna, Naoya; Sugiyama, Shin; Ando, Takuto; Wang, Yefan; Sakuragi, Yuta; Hazumi, Toya; Matsuno, Kohei; Yamaguchi, Atsushi; Nishioka, Jun; Yamashita, Youhei
Citation	Global Biogeochemical Cycles, 36(11), e2022GB007411 <a href="https://doi.org/10.1029/2022GB007411">https://doi.org/10.1029/2022GB007411</a>
Issue Date	2022-11
Doc URL	<a href="http://hdl.handle.net/2115/89113">http://hdl.handle.net/2115/89113</a>
Rights	Copyright 2022 American Geophysical Union.
Type	article
Additional Information	There are other files related to this item in HUSCAP. Check the above URL.
File Information	Glob. Biogeochem. Cycle_36(11)2022.pdf



[Instructions for use](#)

# Global Biogeochemical Cycles®

## RESEARCH ARTICLE

10.1029/2022GB007411

### Key Points:

- Higher nutrient concentrations in a Greenlandic fjord with marine-terminating glaciers were found in 2019 compared to 2018
- Intense summer melting during 2019 led to higher subglacial discharge and enhanced nutrient upwelling
- Intensified upwelling of nutrients into the euphotic zone increased productivity of large diatoms

### Supporting Information:

Supporting Information may be found in the online version of this article.

### Correspondence to:

N. Kanna,  
[nkanna@g.ecc.u-tokyo.ac.jp](mailto:nkanna@g.ecc.u-tokyo.ac.jp)






### Citation:

Kanna, N., Sugiyama, S., Ando, T., Wang, Y., Sakuragi, Y., Hazumi, T., et al. (2022). Meltwater discharge from marine-terminating glaciers drives biogeochemical conditions in a Greenlandic fjord. *Global Biogeochemical Cycles*, 36, e2022GB007411. <https://doi.org/10.1029/2022GB007411>

Received 30 MAR 2022

Accepted 1 NOV 2022

## Meltwater Discharge From Marine-Terminating Glaciers Drives Biogeochemical Conditions in a Greenlandic Fjord

Naoya Kanna<sup>1</sup> , Shin Sugiyama<sup>2,3</sup> , Takuto Ando<sup>4</sup>, Yefan Wang<sup>5</sup> , Yuta Sakuragi<sup>5</sup> , Toya Hazumi<sup>6</sup>, Kohei Matsuno<sup>3,6</sup> , Atsushi Yamaguchi<sup>3,6</sup> , Jun Nishioka<sup>2,3</sup> , and Youhei Yamashita<sup>7</sup> 

<sup>1</sup>Atmosphere and Ocean Research Institute, The University of Tokyo, Chiba, Japan, <sup>2</sup>Institute of Low Temperature Science, Hokkaido University, Sapporo, Japan, <sup>3</sup>Arctic Research Center, Hokkaido University, Sapporo, Japan, <sup>4</sup>Estuary Research Center, Shimane University, Matsue, Japan, <sup>5</sup>Graduate School of Environmental Science, Hokkaido University, Sapporo, Japan, <sup>6</sup>Faculty/Graduate School of Fisheries Sciences, Hokkaido University, Hakodate, Japan, <sup>7</sup>Faculty of Environmental Earth Science, Hokkaido University, Sapporo, Japan

**Abstract** An increasing body of work has shown the potential impacts of subglacial discharge from marine-terminating glaciers on the marine environment around Greenland. Upwelling of nutrients associated with rising buoyant plumes near the front of marine-terminating glaciers plays a key role in maintaining the high productivity of connected fjords. The response of protist communities to subglacial discharges into fjords nevertheless remains poorly understood. Here we show data of water properties, nutrients, and protist communities during two summers in 2018 and 2019 in a Greenlandic fjord system fed by marine-terminating glaciers. This study included the period of intense summer melting of the Greenland Ice Sheet in 2019. The data revealed high nutrient concentrations in 2019 that were attributed to intensified upwelling of nutrients and dissolved iron into the subsurface layer. The source of the iron and the nutrients was subglacial discharge and deep fjord water, respectively. Intense glacial discharges in 2019 mitigated nitrate and phosphate limitations of phytoplankton in the fjord and resulted in an increase of chlorophyll *a* in the subsurface layer and growth of large diatoms. Heterotrophic protists such as dinoflagellates, tintinnids, and nanoflagellates were more abundant in the summer of 2019. We concluded that nutrient upwelling by subglacial discharges was the major driver of the structure of lower trophic levels in fjord ecosystems. We hypothesize that the more intense melting of glaciers and related increase in subglacial discharge will enhance nutrient upwelling, and increased summer productivity in fjords until the glaciers retreat and terminate on land.

## 1. Introduction

Nearly 35% of outlet glaciers of the Greenland Ice Sheet terminate in the ocean (Gardner et al., 2013) where large volumes of freshwater are discharged from the glacier bed, which is situated below sea level. Subglacial discharge and associated upwelling plumes entrain large volumes of saline, warm, deep fjord water (e.g., Rignot et al., 2010). Heat carried by the upwelling plumes induces underwater melting and undercutting of the glacier front, which facilitate loss of ice due to calving (Fried et al., 2015). The increase of frontal ablation during the period of intensive meltwater discharge results in retreat and thinning of the glacier (Carroll et al., 2016; Sutherland et al., 2019). The influence of the ocean is thought to be a driver of the widespread retreat and thinning of marine-terminating glaciers in Greenland (e.g., Cowton et al., 2018; Howat & Eddy, 2011; Straneo & Heimbach, 2013). Changes in the productivity of the fjords associated with the melting and retreat of marine-terminating glaciers have been of great concern in not only Greenlandic fjords (Hopwood et al., 2018; Meire et al., 2017) but also the Arctic fjords of Svalbard (Laufer-Meiser et al., 2021) and the Canadian Arctic Archipelago (Bhatia et al., 2021; Williams et al., 2021) because long-term retreat of the glaciers into shallower water or onto land will reduce upwelling of nutrients. Such a connection between ice-ocean interactions and the productivity of marine ecosystems is not exclusive to the northern hemisphere. Similar observations have been reported at changing glaciers in the Antarctic Peninsula fjord (Cape, Vernet, et al., 2019; Forsch et al., 2021). Previous studies have suggested that glacier retreat will impact marine productivity because the high productivity of proglacial fjords is sustained by the transport of materials by buoyant plumes near the glacier front (Lydersen et al., 2014; Sugiyama et al., 2021).

An important function of the plume in the biogeochemistry of a fjord is the entrainment of nutrient-rich deep fjord water. Fjord circulation driven by the buoyant plume greatly enhances delivery to the euphotic zone of nitrate, the potentially limiting nutrient for phytoplankton throughout summer (Hopwood et al., 2018; Kanna et al., 2018; Meire et al., 2016). The flux of nitrate into Greenlandic fjords from major marine-terminating glaciers has been estimated to exceed  $2 \text{ Gmol yr}^{-1}$ , which is higher than the flux from Arctic rivers to the Arctic Ocean (Cape, Straneo, et al., 2019; Hopwood et al., 2018). Summer production in Greenlandic glacial fjords is strongly influenced by the upwelling of nitrate near the glacier fronts and is therefore affected by the quantity of subglacial discharge (Bhatia et al., 2021) and the depth of the glacier grounding line (Hopwood et al., 2018). The volume of subglacial discharge is highly dependent on climatic conditions. For example, unprecedented atmospheric conditions in July 2019 caused remarkably high surface melting (a mass loss of  $223 \pm 12 \text{ Gt month}^{-1}$ , Sasgen et al., 2020). There has been a trend of rapid warming and increasing occurrence of intensive melt events in Greenland, as well as long term trend of increasing annual meltwater flux (Trusel et al., 2018). However, the impacts of this trend on the nitrate flux into the fjords, summer productivity, and the structure of protist communities are unknown.

Glacial meltwater also delivers large quantities of iron (Fe) to the euphotic zone. Subglacial discharge upwells as a plume that is turbid and rich in Fe (Bhatia, Kujawinski, et al., 2013; Hawkings et al., 2014; Hopwood et al., 2016; Kanna et al., 2020). The plume water subducts beneath a layer of relatively fresh surface water originating from land-terminating glaciers and rivers, resulting in summer phytoplankton blooms at the boundary of the fresh surface layer and subsurface plume water (Kanna et al., 2018; Meire et al., 2017). While the upwelling of nitrate-rich, deep fjord water potentially mitigates the nitrate limitation of phytoplankton, Fe-rich subglacial discharge renders the fjord ecosystem replete with Fe (Hopwood et al., 2016; Kanna et al., 2020). This mechanism is important because Fe-deficiency limits uptake of nitrate by phytoplankton, even though the water contains sufficient amounts of nitrate (e.g., Morel & Price, 2003; Twining & Baines, 2013).

Iron exhibits non-conservative behavior across the salinity gradient in glacial fjords. Significant amounts of glacier-sourced Fe are removed by flocculation and precipitation upon mixing with seawater (Hopwood et al., 2020; Schroth et al., 2014; R. Zhang et al., 2015). The transformation of Fe from particulate to dissolved forms is likely affected by the occurrence of dissolved organic matter (DOM) in the fjord. The DOM in estuarine and coastal waters often includes humic substances (Batchelli et al., 2010; Laglera & van den Berg, 2009). Humic substances are heterogeneous mixtures of organic molecules that form during the decay of biogenic remains, and can function as Fe ligands (Gledhill & Buck, 2012). Humic substances may contribute to the long-range transport of Fe because they prevent the Fe precipitating and flocculating by forming a complex with Fe (e.g., Yamashita et al., 2020). However, the impact of humic substances on the delivery of Fe into glacial fjords has not been quantified.

In this study, we focused on function of the plume in the biogeochemistry of a Greenlandic fjord system fed by marine-terminating glaciers: an entrainment of nutrient-rich water and delivery of Fe. The observations were made during two successive summer seasons of 2018 and 2019. We hypothesized that plume formation during a large melt event in 2019 in Greenland promoted a large amount of upward nitrate flux from deep fjord water as well as Fe flux from subglacial discharge. We evaluated the impact of upwelling plumes on nitrate fluxes and the distribution of protist communities in the fjord by comparing our results from the two summers. In addition to processes related to nitrate, we investigated the linkage of humic substances with Fe in the fjord with a focus on humic-like fluorescent dissolved organic matter ( $\text{FDOM}_H$ ). By combining these datasets, we interpret the impact of subglacial discharge on summer productivity in a fjord system.

## 2. Materials and Methods

### 2.1. Study Area

Inglefield Bredning is an 80-km-long fjord system in northwestern Greenland (Figure 1). The fjord is fed by nine marine-terminating glaciers, which terminate at water depths from approximately 150 to 600 m (Porter et al., 2014; Wang et al., 2021; Willis et al., 2018). Bowdoin Glacier (Kangerluarsuup Sermia in Greenlandic; Bjørk et al., 2015) flows into the 20-km-long Bowdoin Fjord, which connects to Inglefield Bredning (Figure 1). This region has been the focus of intensive field observations targeting glacier–ocean interactions (Sugiyama et al., 2021). Previous studies have reported the impact of subglacial discharge on the marine ecosystem in

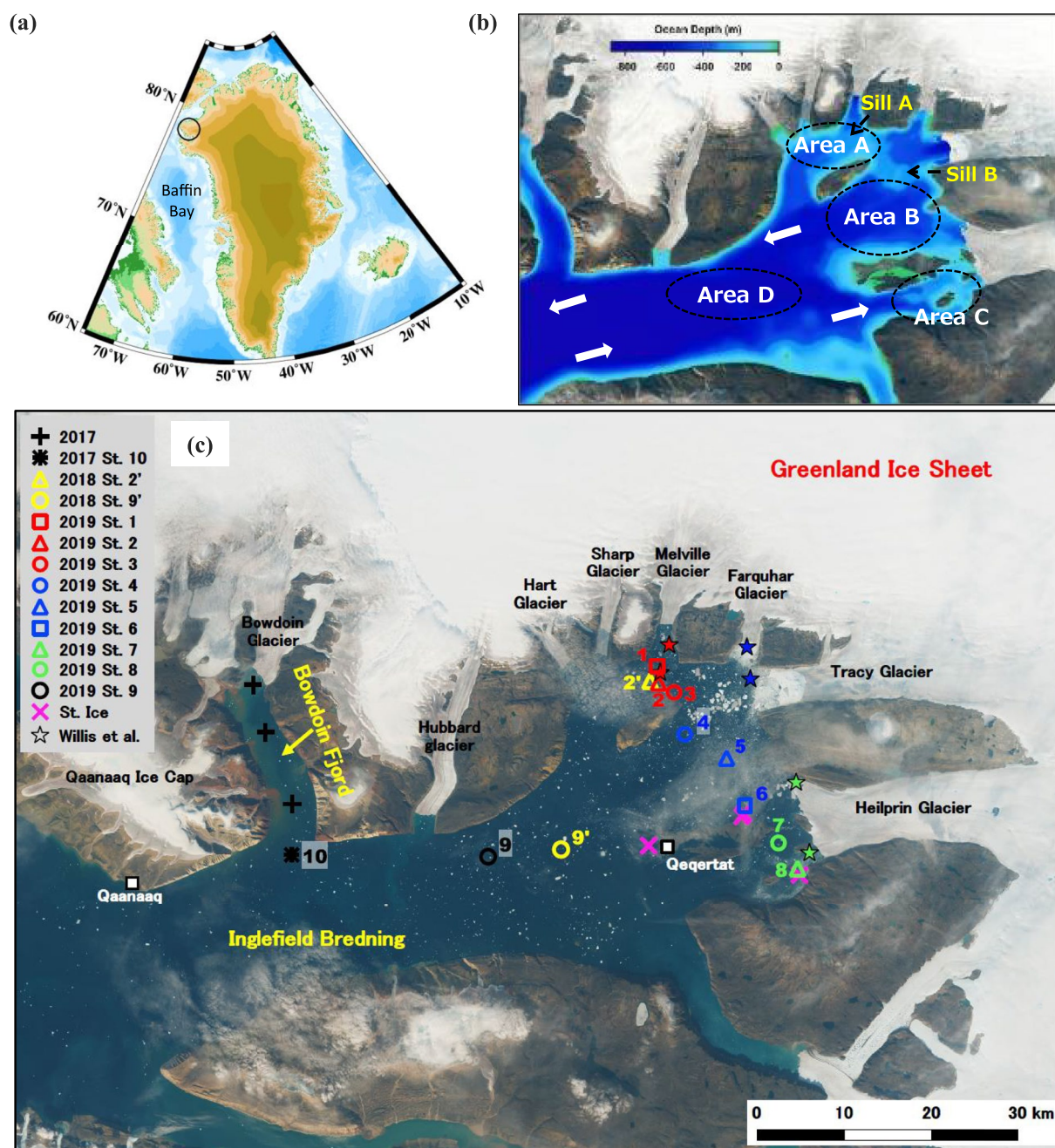


**Figure 1.** (a) Location of the study area in Greenland (circle). (b) Four areas described in the text. White arrows denote the directions of water circulation (Willis et al., 2018). Bathymetric data are taken from Morlighem et al. (2017). (c) Locations of seawater and iceberg sampling in 2017–2019. Hydrographic data near the glaciers (stars) are taken from Willis et al. (2018). The background is a Copernicus Sentinel image acquired on 10 August 2019 and processed with Sentinelflow (<https://github.com/juseg/sentinelflow>).

Bowdoin Fjord (Kanna et al., 2018, 2020; Naito et al., 2019; Nishizawa et al., 2019; Podolskiy & Sugiyama, 2020) and Inglefield Bredning (Matsuno et al., 2020).

## 2.2. Sampling

We used a trace-metal-clean method for sampling seawater (Kanna et al., 2020). Low-density polyethylene (LDPE) bottles (125 mL, Thermo Fisher Scientific), Acropak capsule with supor membrane filters (0.2- $\mu$ m pore size, Pall Corp.) and Teflon-coated 2.5-L Niskin-X samplers (General Oceanics, Inc.) were thoroughly



acid-cleaned in a class-100 clean-air laboratory following a previously reported method (Cutter et al., 2010). Sampling and CTD (conductivity-temperature-depth) casts in Inglefield Bredning were carried out from 12 to 19 August 2019 at nine stations (St. 1–9) (Figure 1c), including two nearby stations that were sampled from 13 to 17 August 2018 (St. 2' and 9'). Data from Bowdoin Fjord in 2017 and Inglefield Bredning in 2018 have been taken from Kanna et al. (2020) and Matsuno et al. (2020), respectively. Seawater samples were collected from a 5-m-long motorboat with the Niskin-X samplers suspended on a Kevlar rope. Teflon-coated messengers were used to close the samplers. Samples for dissolved Fe (dFe) analyses were dispensed into LDPE bottles after filtration through a 0.2- $\mu\text{m}$  Acropak capsule filter attached to spigots of the samplers on board. The samples were transported to Japan and acidified to a pH less than 1.8 by addition of ultrapure hydrochloric acid (Tamapure AA-10, Tama Chemicals) in a clean-air laboratory three weeks after the samples were collected. The acidified samples were stored for 6 months prior to analysis. Samples for dissolved organic carbon (DOC) and FDOM<sub>H</sub> analyses were dispensed into acid-cleaned, 30-mL polycarbonate jars (Thermo Fisher Scientific Inc.) after filtration through a 0.2- $\mu\text{m}$  Acropak capsule filter. Samples for macronutrient and suspended particle analyses were collected into 10-mL acrylic vials (Sanplatec Corp.). Samples for analyses of Chlorophyll *a* (Chl. *a*) were filtered onto a polycarbonate filter (10- $\mu\text{m}$  pore size, Whatman, Inc.) and a glass fiber filter (0.7- $\mu\text{m}$  nominal pore size, Whatman GF/F) under a gentle vacuum ( $<0.013$  MPa). The Chl. *a* was then extracted in *N,N*-dimethylformamide (FUJIFILM, Wako Pure Chemical Corp.) for 2 weeks at  $-20^{\circ}\text{C}$  (Suzuki & Ishimaru, 1990). Samples for microscopic analysis of protist communities were collected into 500-mL plastic bottles and fixed with 1% glutaraldehyde. All samples, except those for the Fe and microscopic analyses, were immediately frozen at  $-20^{\circ}\text{C}$  in a portable freezer and then stored at  $-20^{\circ}\text{C}$  in a freezer room until analysis in Japan.

Eight pieces of floating ice were randomly collected and dispensed into LDPE buckets (6-L capacity, AS ONE Corp.) ("St. Ice" in Figure 1c). The ice samples were identified as originating from icebergs because the  $\delta^{18}\text{O}$  of the ice ( $-27.1 \pm 1.1\text{‰}$ , Appendix Table 1 in Supporting Information S1) was low compared to the value ( $+0.05\text{‰}$ ) reported for sea ice (Alkire et al., 2010). The iceberg samples were melted at ambient temperature on the day of the sampling and immediately filtered with acid-cleaned Millex syringe filters (0.2- $\mu\text{m}$  pore size, Merck Millipore Corp.) for analysis of DOC and FDOM<sub>H</sub>. The meltwater was also subsampled without filtration for macronutrient analysis.

Vertical distributions of water properties in Inglefield Bredning were measured at approximately 2-m intervals by using a CTD sensor (SBE 37-SM, Sea Bird Scientific). The precisions of the conductivity, temperature, and pressure measurements were  $\pm 0.003$  m S  $\text{cm}^{-1}$ ,  $\pm 0.002^{\circ}\text{C}$  and  $\pm 0.1\%$  of full-scale range (350 dbar), respectively. Salinity in seawater was also measured with a salinometer (AUTOSAL 8400B, Guildline Instruments). The measured salinity in grab samples was used for calibration of the CTD sensor.

### 2.3. Sample Analyses

Procedures for analysis of Fe in seawater have been detailed by Kanna et al. (2020). The dFe in seawater samples was preconcentrated with a Nobias Chelate-PA1 resin column (Hitachi High Technologies) (Evans & Nishioka, 2018; Sohrin et al., 2008). The acidified seawater samples were adjusted to pH  $6.0 \pm 0.1$  by addition of a 3.6-M buffer solution prepared from acetic acid and aqueous ammonia. The Fe concentrated onto the resin was eluted with 1-M nitric acid and analyzed with a graphite furnace atomic absorption spectrophotometer (Z-2700, Hitachi High Technologies). All reagents used for the Fe analysis were ultrapure grade. Our pre-concentration process was validated by measuring the Fe concentrations in certified reference materials for trace metals (National Research Council Canada). The measured Fe concentrations in NASS-6 (containing  $0.483 \pm 0.045$   $\mu\text{g kg}^{-1}$ ) and CASS-6 (containing  $1.53 \pm 0.12$   $\mu\text{g kg}^{-1}$ ) were  $0.490 \pm 0.01$   $\mu\text{g kg}^{-1}$  ( $n = 3$ ) and  $1.40 \pm 0.05$   $\mu\text{g kg}^{-1}$  ( $n = 3$ ), respectively.

The DOC analysis was conducted with a total organic carbon analyzer (TOC-V<sub>CSH</sub>, Shimadzu) equipped with a high-temperature combustion furnace. The accuracy and consistency of the measured DOC concentrations were evaluated by analyzing a reference seawater (produced by Dr. D. A. Hansell, University of Miami, Florida, USA). The measured DOC concentration in the reference seawater (containing  $41\text{--}43$   $\mu\text{mol L}^{-1}$ ) was  $41.3 \pm 0.9$   $\mu\text{mol L}^{-1}$  ( $n = 25$ ). The FDOM was analyzed with a spectrofluorometer (Fluoromax-4, Horiba, Ltd.). The excitation emission matrix spectra (EEMs) were scanned with a 0.25-s integration time and collected at excitation wavelengths (Ex) ranging from 250 to 450 nm and emission wavelength (Em) ranging from 290 to 600 nm. EEMs of samples were corrected and calibrated to Raman Unit (RU) according to Tanaka et al. (2014). The FDOM<sub>H</sub> was quantified as the fluorescence intensity at Ex = 320 nm and Em = 420 nm, respectively (Yamashita et al., 2007, 2020). The

fluorescence intensity was calibrated to the area under the water Raman peak of ultrapure water ( $\text{Ex} = 320 \text{ nm}$ ), which was analyzed daily with freshly prepared ultrapure water and calibrated to Raman units ( $\text{RU}_{320}, \text{nm}^{-1}$ ) (Yamashita et al., 2020).

For macronutrient analysis, the frozen samples were thawed at  $4^{\circ}\text{C}$  for 2 days, and then the samples were equilibrated to room temperature before analysis (Macdonald et al., 1986; J.-Z. Zhang & Ortner, 1998). The macronutrient concentrations were measured using an autoanalyzer (QuAatro, BL TEC, Ltd.) with a continuous flow system. The measurements were calibrated with reference seawater materials (KANSO Technos Co., Ltd.). Chl. *a* concentrations were determined with a fluorometer (10-AU, Turner Designs) using the non-acidification method (Welschmeyer, 1994). We used a particle counter (Coulter Multisizer III, Beckman Coulter, Inc.) to determine the concentrations of suspended particles with diameters of  $0.7\text{--}18 \mu\text{m}$ . The  $\delta^{18}\text{O}$  values of the ice samples were determined with an isotope water analyzer (Picarro L2120-i, Picarro, Inc.) with an analytical precision of  $\pm 0.3\text{‰}$ .

The procedures we used for microscopic analyses have been detailed by Matsuno et al. (2020). The 500-mL water samples were stored on a stone table for more than 1 day to allow the protist cells to settle to the bottom of each bottle. The samples were concentrated to 20 mL using a syphon, and then an aliquot of  $0.25\text{--}1.0 \text{ mL}$  was mounted on a glass microscope slide with lines. The micro- and nano-protist communities were counted under an inverted microscope with  $40\text{--}400\times$  magnification and identified to the species/genus level (Evangelopoulos, 2002; Fukuyo et al., 1997; Hasle & Syvertsen, 1997; Maeda, 1997; Taniguchi, 1997). A double-staining method with 4',6-diamidino-2-phenylindole (DAPI) and fluorescein isothiocyanate (FITC) (Sherr & Sherr, 1983) was used to count nanoflagellates in the water samples fixed in 2019. Sub-samples ( $50 \text{ mL}$ ) were gently filtered ( $<80 \text{ mm Hg}$ ) onto black-stained,  $0.8\text{-}\mu\text{m}$  pore size filters (Advantec Corp.) and stained with DAPI and FITC for 15 min. After the staining, the filter was mounted on a glass slide with mounting fluid (FA, VMRD, Inc.). Autotrophic and heterotrophic nanoflagellates on the filter were counted under an epifluorescence microscope (ECLIPSE 80i, Nikon Corp.). For the water samples fixed in 2018, we counted nanoflagellates without distinction. The protist biovolumes were calculated using the measured cell sizes (lengths and widths) (Sun & Liu, 2003). The carbon biomasses were estimated using the carbon–volume relationship (Menden-Deuer & Lessard, 2000). The biomasses ( $\mu\text{gC L}^{-1}$ ) were calculated from the carbon biomass per cell and from the cell abundances (cells  $\text{L}^{-1}$ ).

### 3. Results

#### 3.1. Hydrography

Based on geographical characteristic and similarities of water properties, our 2019 data set was classified into four areas: (a) Area A (Sts. 1–3); (b) Area B (Sts. 4–6); (c) Area C (Sts. 7–8); and (d) Area D (St. 9) (Figures 1b and 1c). Area A is located on a shallow sill (“Sill A” in Figure 1b) in front of the Melville Glacier. Area B is located in a  $\sim 500\text{-m}$ -deep basin south of a sill (“Sill B” in Figure 1b). The Farquhar Glacier, Tracy Glacier, and the northern terminus of the Heilprin Glacier flow into Area B. Area C is located in front of the southern and central termini of the Heilprin Glacier which flows into the fjord through three separate termini. Area D is approximately  $40 \text{ km}$  west from the above-mentioned largest glaciers. Because the influence of glacial discharge was expected to be weaker than that of the other areas, data obtained from Area D were compared to data from the other areas. To compare biogeochemical conditions between 2018 and 2019, data obtained from two stations (St. 2 and 9 for 2019 and St. 2' and 9' for 2018) were used (Figure 1c). Although the distance between St. 9 and 9' is apart (approximately  $8.5 \text{ km}$ ), the both stations are very similar in terms of physical water properties (Willis et al., 2018).

Surface waters in the four areas were relatively fresh and warm (Figures 2a, 2b, 2d, 2e, 2g, and 2h). Characteristics of the waters are derived from ice melt from the Greenland Ice Sheet and peripheral glaciers as well as the atmospheric heating. Minor changes of salinity in the surface water have also been attributed to the melting of sea ice (Kanna et al., 2018). The waters were underlain by Polar Water (potential temperatures ( $\theta$ )  $< -1^{\circ}\text{C}$ , salinity (*S*) close to 33.6) that originated in the Arctic Ocean (Båle et al., 2002; Willis et al., 2018). In the recent literature, Polar Water has been referred to as Baffin Bay Polar Water (Rysgaard et al., 2020). The  $\theta$  in Areas B, C, and D gradually increased with depth and exceeded  $0^{\circ}\text{C}$  in the regions below  $250 \text{ m}$  (Figures 2d and 2g). The water that forms this deep, warmer layer is referred to as Atlantic Water ( $\theta > 0^{\circ}\text{C}$ ,  $S > 34.2$ ), and it originates from the North Atlantic (Båle et al., 2002; Willis et al., 2018). In the recent literature, Atlantic Water has been

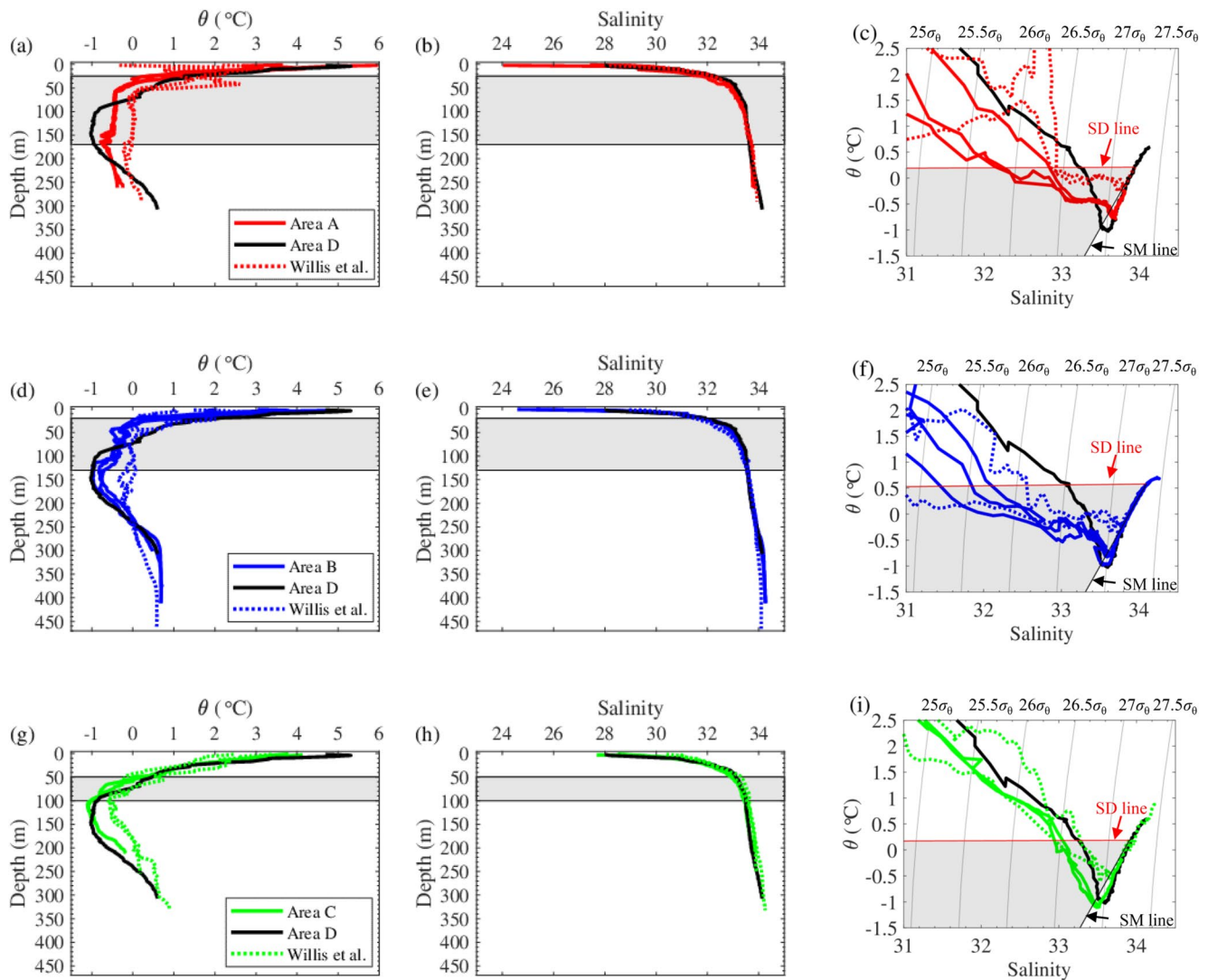


**Figure 2.** Vertical profiles of  $\theta$  and salinity obtained in (a and b) Area A, (d and e) Area B, and (g and h) Area C. Salinity versus  $\theta$  along with isopycnals ( $\sigma_\theta$ ) in (c) Area A, (f) Area B, and (i) Area C. Red and black lines represent mixing lines of seawater with subglacial discharge (SD) and submarine meltwater (SM), respectively. All graphs contain data from Area D for comparison. Shaded area shows the density range of plume water as described in the text.

referred to as Subpolar Mode Water (Rysgaard et al., 2020). In Area A, the  $\theta$  of water below a depth of 250 m was less than 0°C (Figure 2a) because Sill A (Figure 1b) prevents intrusion of Atlantic Water into the region. Analysis of the  $\theta$  versus  $S$  diagram indicated that the properties of the upper water layer (<150 m), which was characterized by density less than  $27.0 \sigma_\theta$ , differed significantly among the four areas (Figures 2c, 2f, and 2i). The differences were most likely due to the magnitude of the mixing of seawater with meltwater supplied by the marine-terminating glaciers. The variations of  $\theta$  and  $S$  were larger in Areas A and B than in Area D. To deduce the relative contribution from submarine meltwater and subglacial discharge on changes in the  $\theta$  and  $S$  of seawater, we used a mixing model of both meltwaters with seawater that has been used by several studies (e.g., Gade, 1979; Kanna et al., 2020; Mankoff et al., 2016; Mortensen et al., 2013; Ohashi et al., 2020; Straneo et al., 2012; Willis et al., 2018). Two mixing lines were plotted on the  $\theta$ – $S$  diagram (Figures 2c, 2f, and 2i). One line corresponds to mixing with submarine meltwater which is from the ice front under the water surface (SM line), and the other to mixing with subglacial discharge water (SD line). The bathymetry near the glacier fronts and CTD data reported by Willis et al. (2018) suggest that the depth of the grounding line is 250 m for the southern and central termini of the Heilprin Glacier, 290 m for the Melville Glacier, and 470 m for the Tracy Glacier. When subglacial discharge and submarine meltwater mix with the seawater near the glacier fronts, the properties of the water are expected to correspond to densities within the ranges bounded by the mixing lines on the  $\theta$ – $S$  diagram (shaded areas in

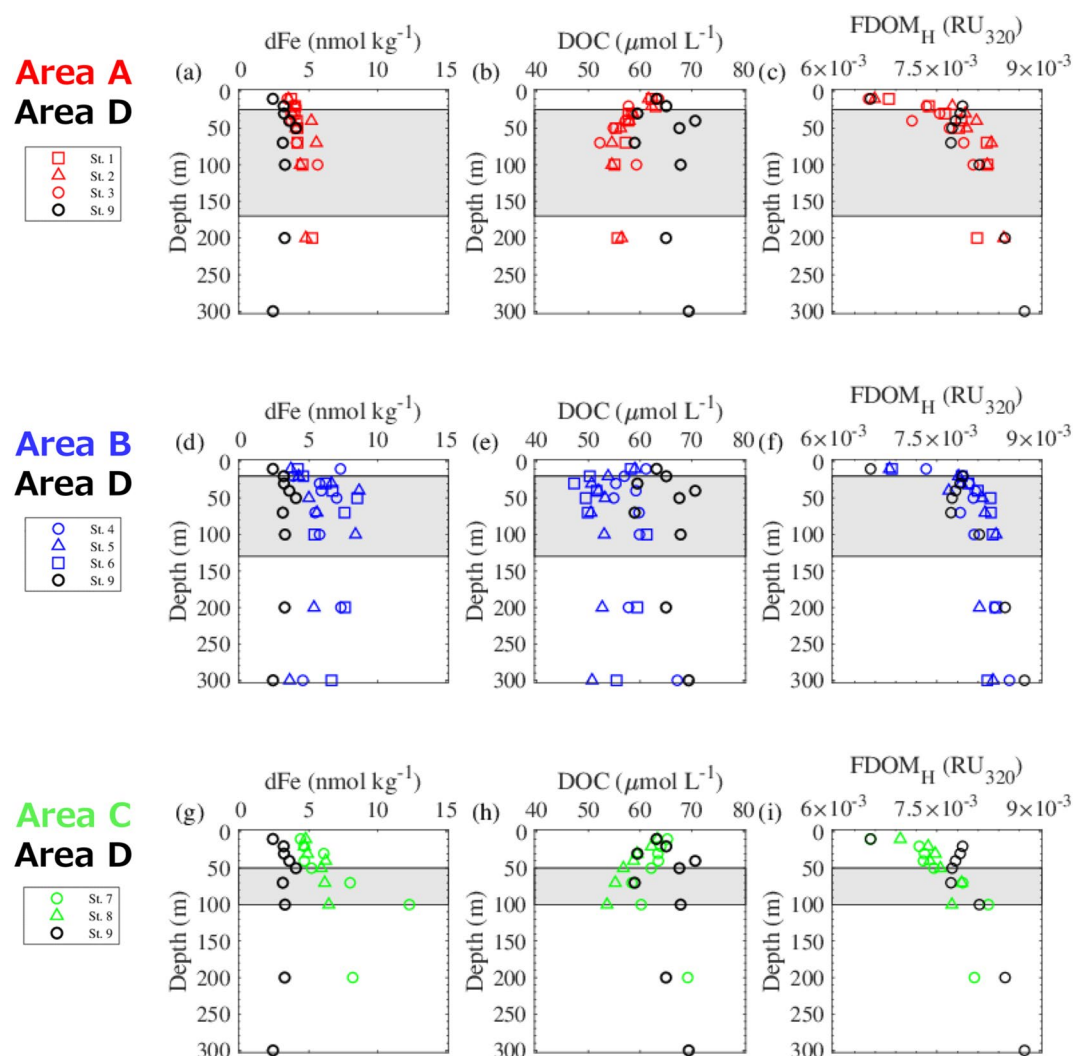


**Figure 3.** Vertical profiles of dFe, DOC, and  $\text{FDOM}_H$  in (a–c) Area A, (d–f) Area B, and (g–i) Area C. All graphs contain data from Area D for comparison. Shaded areas show the depth range of plume water as described in the text.

Figures 2c, 2f, and 2i). We refer to this water as the plume water. The densities of the plume water in Areas A and B were  $25.7\text{--}27.0\ \sigma_\theta$  and  $25.3\text{--}27.0\ \sigma_\theta$ , respectively (Figures 2c and 2f). The density of the plume water in Area C fell within a relatively narrow range of  $26.45\text{--}26.9\ \sigma_\theta$  (Figure 2i). The greater range of the density of the plume water in Areas A and B compared to the other areas indicated that the influence of meltwater was more significant in Areas A and B.

### 3.2. Distributions of dFe, DOC, $\text{FDOM}_H$ , Nutrients, Chl. *a*, and Suspended Particles

In general, dFe concentrations were lower near the surface and gradually increased with depth (Figures 3a, 3d, and 3g). The dFe concentrations in Area D,  $2.4\text{--}4.0\ \text{nmol kg}^{-1}$ , were lower than the concentrations of  $3.4\text{--}12.3\ \text{nmol kg}^{-1}$  near the glaciers (Areas A–C). The DOC concentrations in Area D,  $59\text{--}71\ \mu\text{mol L}^{-1}$ , were higher than the concentrations in other areas below a depth of 40 m (mostly less than  $59\ \mu\text{mol L}^{-1}$ ) (Figures 3b, 3e, and 3h). The  $\text{FDOM}_H$  levels were lowest near the surface and increased with depth in all areas (Figures 3c, 3f, and 3i). The  $\text{FDOM}_H$  levels in the plume water in Areas A and C were positively correlated with the dFe concentrations (Figure 4a) but uncorrelated with the DOC concentrations (Figure 4b). The DOC concentrations in the plume water in Area A were negatively correlated with salinities (Figure 4c). There was a positive correlation between  $\text{FDOM}_H$  and salinity in plume water in Areas A–C (Figure 4d).



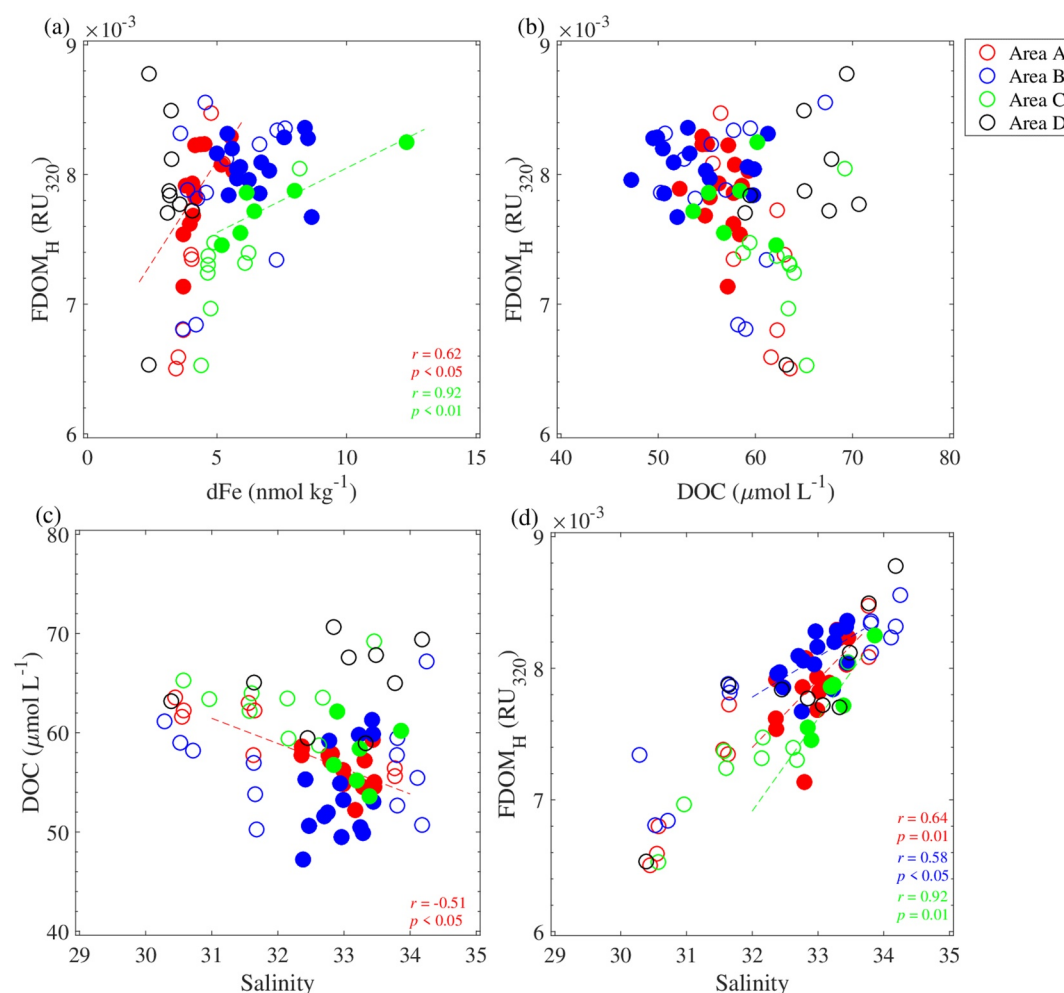


**Figure 4.** Relationships between (a) dFe and  $FDOM_H$ , (b) DOC and  $FDOM_H$ , (c) salinity and DOC, and (d) salinity and  $FDOM_H$  in seawater. Data of plume water are represented by filled markers. Linear relationships were evaluated against the plume water based on Pearson correlation coefficients ( $r$ ). The value of  $FDOM_H$  obtained at depths shallower than 30 m, where light penetration was  $>1\%$  (Appendix Figure 1 in Supporting Information S1), was excluded from the evaluation because of the influence of photochemical degradation.

An increase of the nitrate + nitrite concentrations from near-surface to deeper waters was commonly observed in all areas (Figures 5a, 5g, and 5m). The nitrate + nitrite concentrations in Areas A and B increased rapidly from a depth of 20 m to the deeper regions, and the concentrations at a depth of 20–100 m were notably higher in Areas A and B than in Area D. Vertical distributions of phosphate and silicate concentrations were similar to those of nitrate + nitrite (Figures 5b, 5c, 5h, 5i, 5n, and 5o), except for a slight increase of silicate concentrations near the surface. Silicate can be supplied to the fjord surface from proglacial streams (e.g., Hawkings et al., 2017), but the supply from subglacial meltwater is insignificant because the silicate concentration of iceberg samples was low (Appendix Table 1 in Supporting Information S1). The Chl. *a* concentrations of large phytoplankton ( $>10\ \mu\text{m}$ ) peaked at a depth of 20 m, except for Area C, where the concentration peaked at a depth of 10 m (Figures 5d, 5j, and 5p). The highest concentration of  $6.3\ \mu\text{g L}^{-1}$  was observed in Area B (Figure 5j). The Chl. *a* concentrations of small phytoplankton ( $0.8\text{--}10\ \mu\text{m}$ ) peaked at a depth of 20 m in all areas (Figures 5e, 5k, and 5q). The highest concentration of small phytoplankton, which exceeded  $1\ \mu\text{g L}^{-1}$ , was found in Area D. High environmental levels of suspended particles were present in all areas, but relatively large variations were found below a depth of 50 m in Area B (Figures 5f, 5l, and 5r).

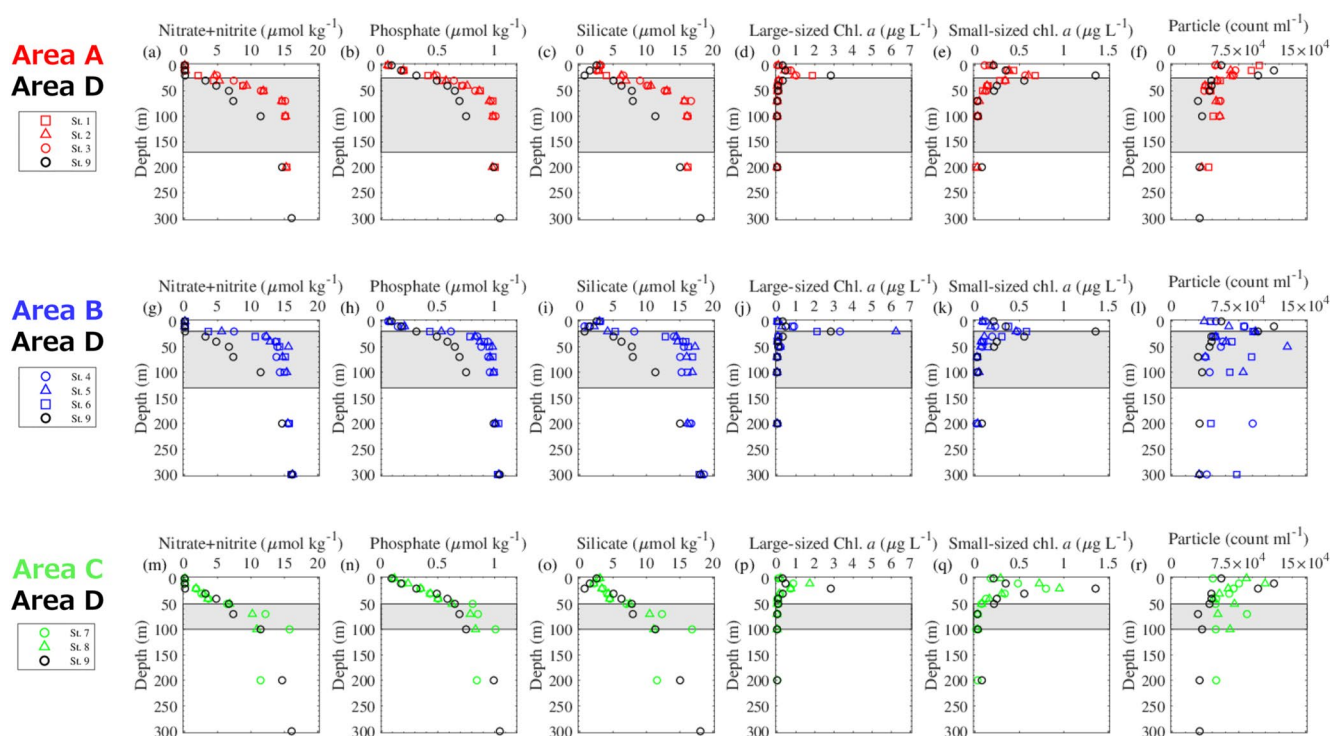


**Figure 5.** Vertical profiles of nutrients, Chl. *a*, and suspended particulate counts in (a–f) Area A, (g–l) Area B, and (m–r) Area C. All graphs contain data from Area D for comparison. Shaded areas show the depth range of plume water as described in the text.

### 3.3. Comparisons Between 2018 and 2019

Water properties within 100 m of the surface showed interannual variations between 2018 and 2019 (Figure 6). In 2019, the salinity (32.3–33.6) of plume water at  $-0.6 < \theta < -0.1^{\circ}\text{C}$  in Area A was significantly lower than the salinity (33.0–33.7) in Area D (Figures 6a–6c). The difference of the salinity was insignificant between Areas A and D in 2018 (Figures 6a–6c).

The water column in Area A was more enriched in dFe in 2019 ( $\sim 5.5 \text{ nM}$ ) than during the summer of 2018 ( $\sim 3.6 \text{ nM}$ ) (Figure 6d). Seawater below a depth of 20 m in Area A was also enriched in nutrients in 2019 (Figures 6e, 6f, and 6g). Even at a distance from the glaciers in Area D ( $>40 \text{ km}$ ), the concentrations of nitrate + nitrite and silicate were relatively high below a depth of 30 m in 2019 (Figures 6e and 6g). Whereas the nitrate + nitrite concentrations were almost at the limit of detection at depths of 0–10 m in both years (Figure 6e), the concentrations of silicate and phosphate were well above the corresponding limits of detection at the same depths (Figures 6f and 6g). The surface layer was relatively depleted in phosphate but slightly enriched in silicate in 2019. The Chl. *a* concentrations in Area D were notably high in 2019 and reached  $4.2 \mu\text{g L}^{-1}$  at a depth of 20 m (Figure 6h). This concentration was nine times the concentration measured in the same area in 2018. The Chl. *a* concentration in Area A in 2019 was 3.4 times the concentration in the same area in 2018 (Figure 6h).

Vertical distributions of protist communities also differed between the 2 years (Figure 7). In 2019, there was a greater variety of micro-protist taxa in the surface layer (0–20 m) (Figures 7a–7d). The integrated biomass of the whole micro-protist community within the surface layer in 2019 was  $320 \text{ mg C m}^{-2}$  in Area A and  $452 \text{ mg C m}^{-2}$  in Area D. Diatom taxa (mostly *Thalassiosira* spp. and *Chaetoceros* spp.) were observed only in 2019 at the two areas (Figures 7b and 7d). The biomass of nanoflagellates in Area A was several orders of magnitude higher in 2019 than in 2018 (Figures 7e and 7f), whereas the biomasses in both years were similar in Area D (Figures 7g and 7h). Heterotrophic nanoflagellates accounted for 89% of the total nano-protist biomass in 2019. The biomass of nanoflagellates significantly correlated to the Chl. *a* concentration in 2019 (Pearson correlation coefficients ( $r$ ) = 0.71,  $p < 0.01$ ), but not in 2018.

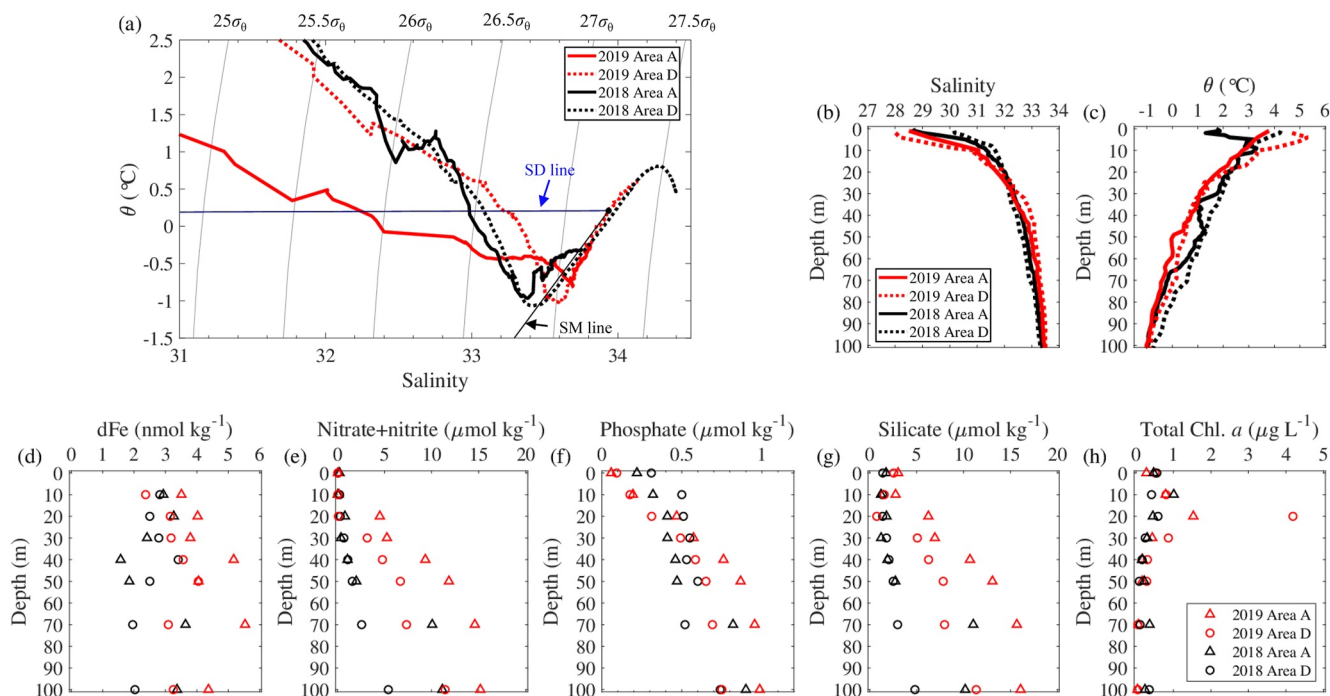


**Figure 6.** Comparison of (a)  $\theta$  versus salinity along with isopycnals ( $\sigma_\theta$ ), (b and c) water properties, and (d–h) biogeochemical components obtained in 2018 and 2019. Blue and black lines in (a) represent mixing lines of seawater with subglacial discharge and submarine meltwater for Area A, respectively.

## 4. Discussion

### 4.1. Distribution of Plume Water in the Fjord

The water mass structures reported by Willis et al. (2018) indicate that water at depths of 75–175 m near Farquhar and Tracy Glaciers is noticeably warmer than water at similar depths more than 20 km off the glaciers

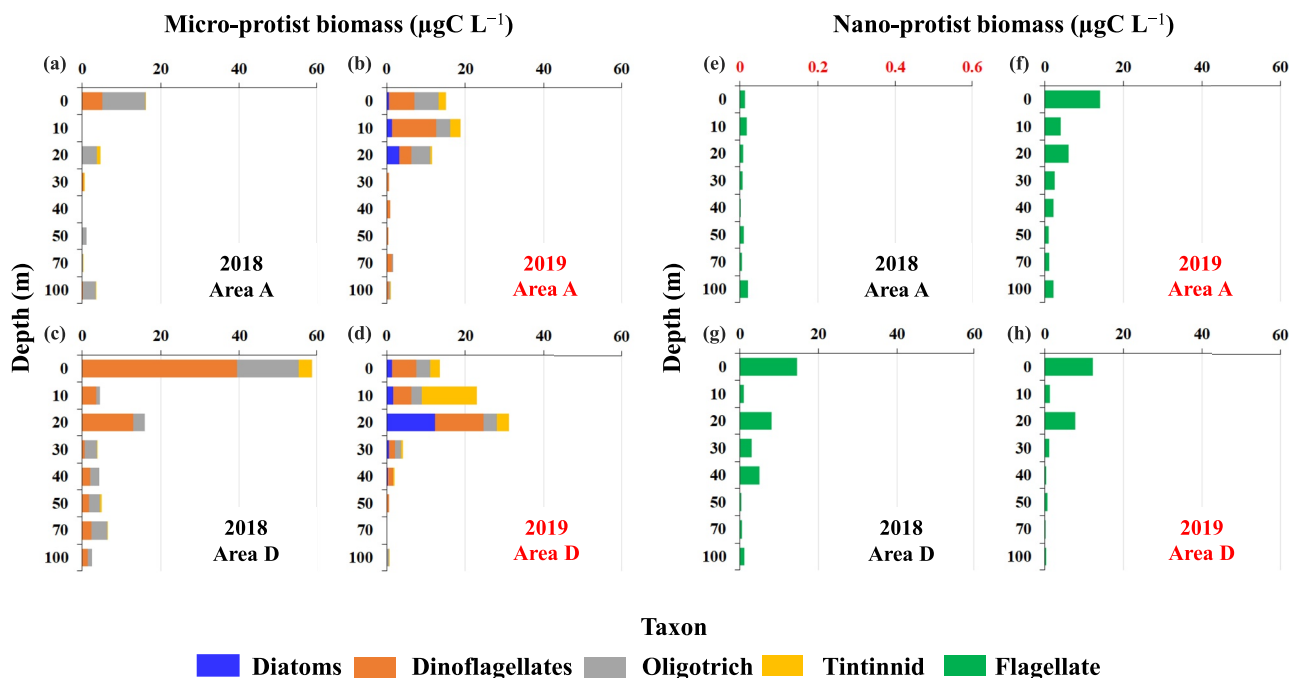


**Figure 7.** Comparison of (a–d) micro-protist biomass and (e–h) nano-protist biomass obtained in 2018 and 2019. Note that the scale of the x-axis in (e) is different from the others.

(see Figure 5 in Willis et al., 2018). This warm layer is formed by upward transport and mixing of warmer and saltier deep waters by rising subglacial discharges. Our observations were consistent with their observations and interpretations. The counterclockwise circulation pattern in Inglefield Bredning moves subglacial water away from the terminus of the Farquhar and Tracy Glaciers and affects the  $\theta$  distribution in Areas A and B. Discharges from the Melville Glacier affect the  $\theta$  distribution in Area A. The  $\theta$  profiles obtained in Areas A and B revealed warm water at depths of 80–170 m (Figure 2a) and 80–140 m (Figure 2d). The indication was that plume water was warmer in these areas compared to Area D. In contrast, water at depths of 20–80 m was colder in Areas A and B. The  $\theta$  values of plume waters were relatively uniform throughout all depths (Figures 2a and 2d). Moreover, the salinities of the plume waters of Areas A and B changed rapidly on the  $\theta$ – $S$  diagram (Figures 2c and 2f), that is, the salinity decreased along a line parallel to the SD line. We attributed the changes of salinity to mixing of seawater with subglacial discharge, as reported in previous studies in this region (Kanna et al., 2020; Ohashi et al., 2020; Willis et al., 2018). The conclusion of our water mass analysis was that the properties of the water sampled in Areas A and B indicated mixing of fjord water with subglacial discharge water upwelled to a depth of ~20 m.

In contrast to Areas A and B, a layer of relatively warm water was not apparent in the plume water of Area C, although a layer of cold water (relative to Area D) was apparent at depths of 50–100 m (Figure 2g). The tendency of the  $\theta$  and  $S$  values to lie along a line parallel to the SD line was less apparent in Area C than in Areas A and B (Figure 2i). This observation is also consistent with the previous study in this region (Willis et al., 2018). We expect that Area C did not capture the subglacial discharge from Heilprin Glacier due to counterclockwise circulation in Inglefield Bredning. As shown in Figure 1b, currents from outside of Inglefield Bredning flow along southern shore before circulating past Heilprin, Tracy, and then exiting along the northern shore (Willis et al., 2018). Area C is located upstream of these glaciers in terms of the direction of the water currents and therefore there is less ocean-ice interaction compared to Areas A and B.

#### 4.2. Distributions of DOC, FDOM<sub>H</sub>, and dFe

In order to evaluate sources of DOM in Inglefield Bredning, fluorescence indices were calculated from the ratio of fluorescence emission intensity at a shorter and longer wavelength at a fixed excitation wavelength. The fluorescence index (FI,  $E_m = 470/520$  nm at  $E_x = 370$  nm) is thought to distinguish between terrestrial and soil sources ( $FI < 1.4$ ) and aquatic and microbial sources ( $FI > 1.9$ ) of organic matter (Birdwell & Engel, 2010; Cory & McKnight, 2005; Huguet et al., 2009). The biological index (BIX,  $E_m = 380/430$  nm at  $E_x = 310$  nm) has been used to distinguish between detrital (allochthonous) sources ( $BIX < 0.6$ ) and freshly produced (autochthonous) sources ( $BIX > 0.8$ ) of organic matter (Birdwell & Engel, 2010; Cory & McKnight, 2005; Huguet et al., 2009). The FI and BIX values were not estimated for the iceberg samples because these samples contain relatively large errors due to low DOC concentration (Appendix Table 1 in Supporting Information S1). For the seawater samples, the FI ranged from 1.6 to 1.9, indicating that DOM in Inglefield Bredning may be a mixture of organic matter from terrestrially and microbially sources. The BIX values ranged from 0.98 to 1.2. Given that the BIX in the seawater was larger than 0.8, DOM in Inglefield Bredning is freshly produced DOM.

The relationships between DOC concentrations and salinities in Inglefield Bredning are less clear (Figure 4c) compared to other coastal environments (e.g., Cao et al., 2016; Yamashita et al., 2011). The supply of DOC from subglacial discharge is not likely significant in Inglefield Bredning because DOC concentrations in glacial meltwaters around Greenland are usually low relative to seawater. For example, the DOC concentration is lower in supraglacial water ( $12\text{--}30\text{ }\mu\text{mol L}^{-1}$ , Bhatia et al., 2010; Bhatia, Das, et al., 2013; Holland et al., 2019; Lawson et al., 2014), snow ( $16\text{ }\mu\text{mol L}^{-1}$ , Lawson et al., 2014) and icebergs ( $9.4 \pm 4.6\text{ }\mu\text{mol L}^{-1}$ , Appendix Table 1 in Supporting Information S1) than in fjord water ( $\sim 70\text{ }\mu\text{mol L}^{-1}$ , Figures 3b, 3e, and 3h;  $\sim 130\text{ }\mu\text{mol L}^{-1}$ , Paulsen et al., 2017, 2019). While the DOC concentrations in subglacial discharge from land-terminating glaciers are variable from  $<10$  to  $100\text{ }\mu\text{mol L}^{-1}$ , most of the measurements taken at peak melt in July and August are at the lower end of this value (Bhatia et al., 2010; Bhatia, Kujawinski, et al., 2013; Kellerman et al., 2020; Lawson et al., 2014; Pain et al., 2020; Paulsen et al., 2019). Moreover, the positive correlations between the levels of FDOM<sub>H</sub> and salinity in the plume water, irrespective of sampling areas (Figure 4d), indicated dilution of the plume water endmember by a glacial meltwater endmember. FDOM<sub>H</sub> has been used for several decades to trace terrestrial organic matter in the ocean (e.g., Coble, 1996; Walker et al., 2009). For example, an inverse linear



**Table 1**

*Summary of Vertical Gradients and Mean Brunt–Väisälä (BV) Frequency Squared in the Nitracline in Areas A–D and Bowdoin Fjord*

	Approx. distance from glacier(s) (km)	Nitracline depth ( $dz$ , m)	Nitracline concentration ( $d(\text{NO}_3^- + \text{NO}_2^-)$ , $\mu\text{mol}$ $\text{kg}^{-1}$ )	Vertical gradient of nitrate + nitrite ( $d(\text{NO}_3^- + \text{NO}_2^-)/dz$ , $\text{mmol}$ $\text{m}^{-4}$ )	Mean BV frequency squared in nitracline ( $N^2$ , $10^{-4} \text{ s}^{-2}$ )
Area A	8	20–50	2.1–11.9	0.21–0.34	4.1–5.5
Area B	20	20–50	3.6–15.6	0.21–0.35	3.5–3.9
Area C	4	20–50	1.7–6.8	0.15–0.16	3.9–4.1
Area D	40	20–50	0.1–6.7	0.21	3.6
Bowdoin <sup>a</sup>	1	0–20	0.1–11.5	0.57	49

<sup>a</sup>Kanna et al. (2020).

relationship between the levels of  $\text{FDOM}_H$  and salinities in the North Atlantic have been attributed to terrestrial  $\text{FDOM}_H$  supplied directly from surrounding continents (Jørgensen et al., 2011) as well as from large Arctic rivers via the Arctic Ocean (Amon & Budéus, 2003; Benner et al., 2005; Opsahl et al., 1999). Our data showed trends that differed from those in the North Atlantic.

Here, we discuss relationships between  $\text{FDOM}_H$  and dFe concentrations in Inglefield Bredning. Vertical profiles of water temperature indicate that Polar Water ( $<0^\circ\text{C}$ ) that had originated in the Arctic Ocean is distributed at depths of 50–200 m in Inglefield Bredning (Figures 2a, 2d, and 2g). In the Arctic Ocean, complexes of Fe-humic substances (Fe-HS complexes) account for approximately 80% of dFe concentrations, and concentrations of Fe-HS complexes are highly correlated with  $\text{FDOM}_H$  as well as dFe concentrations (Laglera et al., 2019). Such Fe-HS complexes are thought to be exported from the Arctic Ocean to the North Atlantic (Laglera et al., 2019) and probably to Baffin Bay. The relationships between  $\text{FDOM}_H$  and dFe in the layer of Polar Water are less clear, suggesting that Arctic-origin Fe-HS complexes are not among the major factors that control dFe concentrations in Inglefield Bredning. On the other hand, we found a significant correlation between the  $\text{FDOM}_H$  levels and dFe concentrations in the plume waters of Areas A and C (Figure 4a). The result indicated that  $\text{FDOM}_H$  in glacial meltwater may be an important determinant of the dFe concentration in Areas A and C. The BIX values suggest that  $\text{FDOM}_H$  in Inglefield Bredning is freshly produced DOM. Although a high contribution of microbially derived DOM in glacial meltwaters has been reported in elsewhere (e.g., Kellerman et al., 2020; Marshall et al., 2021; Pain et al., 2020), its contribution in our studied fjord is unclear. The absence of a significant correlation between dFe and  $\text{FDOM}_H$  in the plume water of Area B (Figure 4a) was probably due to the high concentration of suspended sediment (Figure 5l) and removal of  $\text{FDOM}_H$  by adsorption onto sediment particles. Alternatively, Fe nanoparticles ( $<0.2 \mu\text{m}$ ) might have overwhelmed the organically bound Fe species. Further studies are needed to understand the influence of organic matters on Fe speciation in proglacial fjords.

#### 4.3. Influence of Subglacial Discharge on Nutrient Concentrations and dFe Distributions in the Fjord

The plume waters in Areas A and B were strongly influenced by subglacial discharge, whereas its influence on the water in Area C was relatively weak. To quantify the flux of nitrate supplied from the plume water to the near-surface layer ( $\sim 20\text{-m}$  depth) in Areas A–D, we compared the vertical gradients of the nitrate + nitrite concentrations ( $d(\text{NO}_3^- + \text{NO}_2^-)/dz$ ) which are an important metric of nitrate diffusion (Nishioka & Obata, 2017). An example in Bowdoin Fjord is that the  $d(\text{NO}_3^- + \text{NO}_2^-)/dz$  at a station 1 km off the terminus of Bowdoin Glacier (Figure 1c) was steep at depths of 0–20 m (Table 1). This steep gradient reflects that an upwelling plume distributes nitrate-enriched water into the near-surface layer in Bowdoin Fjord (Kanna et al., 2018, 2020). In Inglefield Bredning, the  $d(\text{NO}_3^- + \text{NO}_2^-)/dz$  was the highest in Area B followed by Area A (Table 1). The gradient was relatively small in Areas C and D (Table 1). We deduced that the steep gradients in Areas A and B were due to intrusions of an upwelling plume water.

In addition to the  $d(\text{NO}_3^- + \text{NO}_2^-)/dz$ , the flux of nitrate is inversely proportionate to the Brunt–Väisälä frequency ( $N$ ) wherein the flux is proportionate to the turbulent kinetic energy dissipation ( $\epsilon$ ) in seawater (Osborn, 1980). The  $N$  is an important metric of oceanic vertical stability. The low  $N^2$  value in the nitracline in Areas B and D

indicated weak stratification (Table 1) compared to the near-surface layer of the fjord ( $N^2 > 10^{-3} \text{ s}^{-2}$ , Appendix Figure 2 in Supporting Information S1). Because the  $N^2$  values in Areas B and D were comparable, the relative magnitudes of the flux of nitrate would depend on the values of  $\epsilon$  and  $d(\text{NO}_3^- + \text{NO}_2^-)/dz$ . A recent study has reported relatively low values of  $\epsilon$  ( $\sim 10^{-9} \text{ W kg}^{-1}$ ) in the upper  $\sim 200 \text{ m}$  in proglacial fjords along northwest Greenland, except for a high value of  $\epsilon$  ( $\sim 10^{-7} \text{ W kg}^{-1}$ ) near the front of a marine-terminating glacier ( $< 2 \text{ km}$ ) (Bendtsen et al., 2021). Although no measurement of  $\epsilon$  has been performed in Inglefield Bredning, the value of  $\epsilon$  may have been greater in Area B because of the influence of subglacial discharge.

Overall, the flux of nitrate + nitrite is expected to be the highest in Area B, which is characterized by weak stratification and a steep gradient of nitrate + nitrite concentrations. The highest abundance of large phytoplankton was found near the surface in Area B (Figure 5j), which is likely associated with the high flux of nitrate + nitrite. The lower abundance of large phytoplankton in Area A (Figure 5d) may be associated with the smaller flux of nitrate + nitrite because of the stronger stratification of the fjord ( $N^2$ : Area A > Area B, Table 1). We note that the interplay between light availability and the flux of nitrate + nitrite is also important as a determinant for abundance of phytoplankton.

Subglacial discharge plays a key role in the supply of Fe to the fjords because glacial meltwater is rich in Fe (Bhatia, Kujawinski, et al., 2013; Hawkings et al., 2014, 2018; Kanna et al., 2020). In order to quantify Fe derived from subglacial discharge, we calculated the differences of dFe and nitrate + nitrite concentrations (hereafter Fe-diff and N-diff, respectively) on the same isopycnals in seawater at stations between near and far from the glaciers. An example in Bowdoin Fjord is that Fe-diff and N-diff is computed by subtracting the concentrations at St. 10 from those at stations within the Bowdoin Fjord (indicated by “+” in Figure 1c), respectively. The relatively high Fe-diff ( $> 5 \text{ nmol kg}^{-1}$ ) and N-diff ( $\sim 10 \text{ } \mu\text{mol kg}^{-1}$ ) within the density range of plume water indicated the influence of subglacial discharge from Bowdoin Glacier (Figure 8a). The median value of Fe-diff ( $7.0 \text{ nmol kg}^{-1}$ ) peaked within 15 km from the Bowdoin Glacier (Figure 8e). In the same manner, value of Fe-diff and N-diff was calculated for Areas A–C by subtracting the concentrations at St. 9 (Area D) from those at stations within Inglefield Bredning on the same isopycnals. The N-diff values of the plume water in Areas A and B were as much as  $9 \text{ } \mu\text{mol kg}^{-1}$  (Figures 8b and 8c) reflecting the significant influence of subglacial discharge on nitrate + nitrite enrichment of the subsurface layer. The N-diff in Area C was somewhat low ( $\sim 5 \text{ } \mu\text{mol kg}^{-1}$ ) in the plume water (Figure 8d). The Fe-diff of plume water was  $0\text{--}2 \text{ nmol kg}^{-1}$  in Area A,  $1\text{--}5 \text{ nmol kg}^{-1}$  in Area B, and  $2\text{--}9 \text{ nmol kg}^{-1}$  in Area C (Figures 8b–8d). The Fe-diff was expected to be high near a glacier because a significant portion of the Fe is removed after subglacial discharge mixes into the fjord water (Hopwood et al., 2020; Kanna et al., 2020; Krause et al., 2021). In Area C, the median value of Fe-diff in the plume water was  $3 \text{ nmol kg}^{-1}$  within 4 km of the Heilprin Glacier (Figure 8e). However, the median value in Area B ( $2.6 \text{ nmol kg}^{-1}$ ) was greater compared to the value in Area A ( $0.7 \text{ nmol kg}^{-1}$ ) (within 8 km of the Melville Glacier), even though Area B was located approx. 20 km off the Tracy and Farquhar Glaciers (Figure 8e). Because the dFe exhibits non-conservative behavior across salinity gradients (e.g., Hopwood et al., 2020), the net and gross fluxes of dFe from the glaciers into the fjord were presumably different. Nevertheless, we deduced that the higher Fe-diff in Area B was associated with the larger amount of Fe supplied by the subglacial discharges of the Tracy and Farquhar Glaciers.

#### 4.4. Impact of the Intense Summer Melting During 2019 on Nutritional and Biological Conditions in the Fjord

The unusual atmospheric pattern in the summer of 2019 led to the largest melt event ever observed for the Greenland Ice Sheet (Sasgen et al., 2020; Tedesco & Fettweis, 2020). Summer mean air temperatures in Northwestern Greenland were  $4^\circ\text{C}$  warmer in 2019 than in 2018 (Appendix Figure 3a in Supporting Information S1). A significant amount of meltwater ( $\sim 2,000 \text{ m}^3 \text{ s}^{-1}$ ) was also discharged from Northwestern Greenland, which was estimated from two regional climate models ( $77.3\text{--}77.9^\circ\text{N}$  and  $65.0\text{--}70.0^\circ\text{W}$  gridded regions, Mankoff et al., 2020) (Appendix Figure 3c in Supporting Information S1). Runoff from Qaanaaq Glacier, an outlet glacier of the Qaanaaq Ice Cap (Figure 1c) was several times greater in 2019 than in 2018 (Kondo et al., 2021) (Appendix Figure 3b in Supporting Information S1). Since glacial meltwaters are not significant sources of nitrate and phosphate (Hopwood et al., 2020; Kanna et al., 2018, 2020; Meire et al., 2017), large discharges of glacial meltwater might therefore be expected to cause a dilution of nutrient concentrations in surface waters. Sea ice covering Inglefield Bredning also disappeared approximately a week earlier in 2019 than in 2018 (Appendix Figure 4 in Supporting Information S1). The earlier melting of sea ice is considered to lead to earlier initia-

**Table 2**  
Comparison of Biomass of Protist Community Taxa in Chl. *a* Maximum Layer Based on Data Obtained in 2018 and 2019

Taxon	Trophic	2018		2019	
		Area A ( $\mu\text{gC L}^{-1}$ )	Area D ( $\mu\text{gC L}^{-1}$ )	Area A ( $\mu\text{gC L}^{-1}$ )	Area D ( $\mu\text{gC L}^{-1}$ )
Diatoms	Autotrophic	0	0	3.2	12.4
Dinoflagellates	Mixotrophic/Heterotrophic	0.01	13	3.1	12.2
Oligotrich	Heterotrophic	3.7	2.9	4.7	3.4
Tintinnids	Heterotrophic	1.0	0	0.5	3.1
Nanoflagellates	Autotrophic/Heterotrophic	0.008	6.1	8.0	7.8

tion of phytoplankton blooms because phytoplankton can acquire light, resulting in the depletion of nutrients in seawater in early summer. However, in the summer of 2019, nutrients and dFe in seawater remained more abundant compared to 2018 (Figures 6d–6g). Here we highlight how protist community distributions in plume water differed between the two summers.

The lower salinities at depths shallower than 30 m in Areas A and D (Figure 6b) in 2019 indicated that the inputs of freshwater to the fjord were greater in 2019 than in 2018 at the time of sampling. The  $\theta$ – $S$  data from Area A were aligned parallel to the SD line on the  $\theta$ – $S$  diagram in 2019 (Figure 6a). The properties of the water in 2019 varied along the SD line under the influence of subglacial discharge. The changes of  $\theta$  and  $S$  were smaller for the sampled water in Area A in 2018 (Figure 6a). This observation confirmed that the subglacial discharge and its influence on the fjord were greater in 2019 than in 2018 at the time of sampling.

The subglacial discharge led to larger vertical fluxes of nutrients and dFe from the deeper layer to 20 m in 2019 (Figures 6d–6g). Most likely, the subglacial discharge alleviated nitrate limitation of phytoplankton growth. The stimulation of phytoplankton growth in 2019 was implied by the formation of a Chl. *a* maximum layer (CML) at a depth of 20 m (Figure 6h) and by depletion of nitrate + nitrite concentrations in the CML in Area D (Figure 6e). The existence of the CML was more obvious in Area D, probably because the light required for phytoplankton growth was more available in Area D compared to Area A. The total Chl. *a* concentration in the CML in Area D was up to sevenfold greater in 2019 than in 2018, and the Chl. *a* of large phytoplankton accounted for 68% of the total Chl. *a* in 2019 (Figures 5d, 5j, and 5p). Because of their relatively low cell surface area-to-volume ratios, the growth of large phytoplankton is more sensitive to Fe and nutrient deficiencies than that of small phytoplankton (Sunda & Huntsman, 1997; Timmermans et al., 2004). Large phytoplankton thus grew faster than small phytoplankton in 2019.

Among large phytoplankton, diatoms are the predominant contributors to carbon fixation globally and account for 40% of the total primary production in the ocean (Sarhou et al., 2005). Subglacial discharges and upwelling plumes also supplied phosphate into the subsurface euphotic zone and stimulated silicate consumption by large diatoms in 2019. The diatoms (mostly *Thalassiosira* spp. and *Chaetoceros* spp.) in the CML accounted for 28% and 40% of the total micro-protist biomass in Areas A and D, respectively (Figures 7a–7d and Table 2). On the other hand, the diatoms did not thrive at both areas in 2018. Although the dFe, nitrate + nitrite, and silicate concentrations were lower in 2018, they were not likely limiting for diatoms in 2018 because the dFe:N and Si:N ratios at a depth of 30 m (just below CML) were higher than the reported nutrient uptake and elemental composition ratios of diatoms (Table 3). It is worthy to mention that the dFe:N ratio ( $>0.2$ ) in the water column at both areas in 2018 (Figure 9a) was an order of magnitude greater than the phytoplankton cellular Fe:N ratio of 0.03 (Ho et al., 2003; Kanna et al., 2020; Maldonado & Price, 1996; Sunda & Huntsman, 1995; Twining et al., 2004). The result from the dFe:N ratio in the seawater suggests that the seawater within Inglefield Bredning is dFe replete with respect to other phytoplankton demand as well as diatoms. However, N:P and Si:P ratios at stations in 2018 were much lower than the values reported for diatoms (Table 3), and thus the ratios in seawater were not favorable to the growth of diatoms in 2018. The high abundances of heterotrophic dinoflagellates and tintinnids in the CML in 2019 (Table 2) created high grazing pressure on diatoms and nanoflagellates. We nevertheless expected that diatoms would grow at greater depths in the euphotic zone after the period of observations in 2019 because the high N:P and Si:P ratios are available below a depth of 20 m (Figures 9b and 9d). This observation

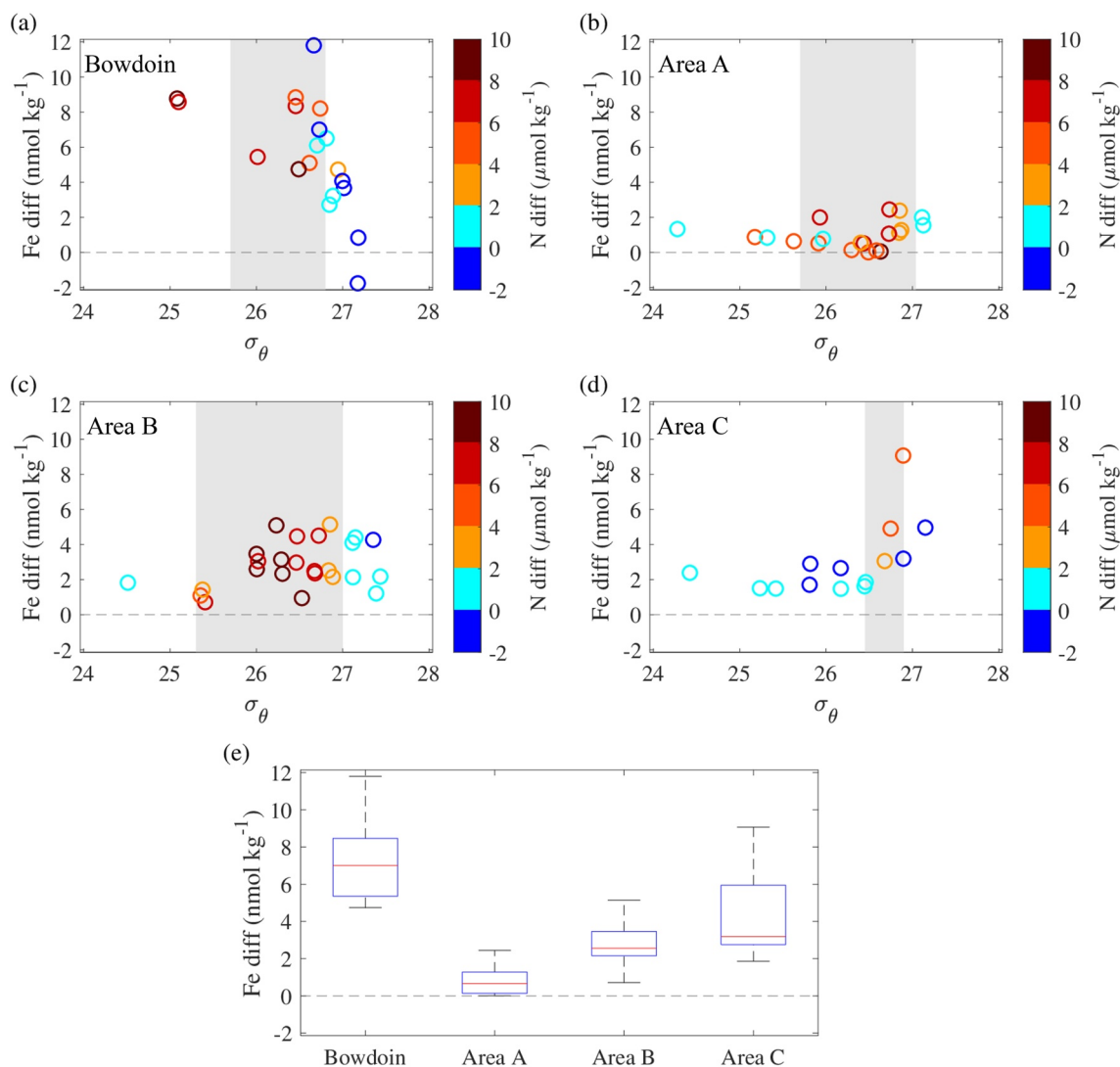


**Figure 8.** (a–d) Relationships among density ( $\sigma_\theta$ ), Fe-diff, and N-diff (indicated by the color scale) in seawater. The Fe-diff and N-diff in (a) was computed by subtracting dFe and nitrate + nitrite concentrations at St. 10 from those at stations within the Bowdoin Fjord on the same isopycnals, respectively. The Fe-diff and N-diff in (b–d) was computed by subtracting the concentrations at St. 9 from those at stations within each area on the same isopycnals, respectively. Shaded area shows the density range of plume water as described in the text. (e) Box plot of Fe-diff in plume water. The bottom and top of the box indicate the 25th and 75th percentiles, respectively, and the line inside the box indicates the median. The bottom and top error bar show minimum and maximum values, respectively.

**Table 3**

Comparisons of dFe and Nutrient Ratios in Seawater, Nutrient Uptake Ratios From Culture Experiments, and Elemental Composition Ratios of Diatoms

	dFe and nutrient ratios in seawater at depth of 30 m				Nutrient uptake ratios from culture experiments <sup>a</sup>			Elemental composition ratios of diatoms <sup>b</sup>
	2018		2019					
	Area A	Area D	Area A	Area D	<i>Thalassiosira</i>	<i>Chaetoceros</i>	Other diatoms	
N:P (mol mol <sup>-1</sup> )	0.9	1.2	9.2	6.4	2.6–13.2	5.4–9.7	5.7–18	10 ± 4
Si:P (mol mol <sup>-1</sup> )	3.0	3.2	12	10	3.7–21	7.1–11.6	12.2–29.9	5.9 ± 1.3
Si:N (mol mol <sup>-1</sup> )	3.2	2.6	1.3	1.6	0.3–2.8	0.7–1.6	1.1–2.2	0.8 ± 0.3
dFe:N (mmol mol <sup>-1</sup> )	6.4	4.1	0.7	1.0	0.48	–	–	ca. 0.23

<sup>a</sup>Takeda (1998), Kudo (2003), Timmermans et al. (2004), and Price (2005). <sup>b</sup>Sarthou et al. (2005).



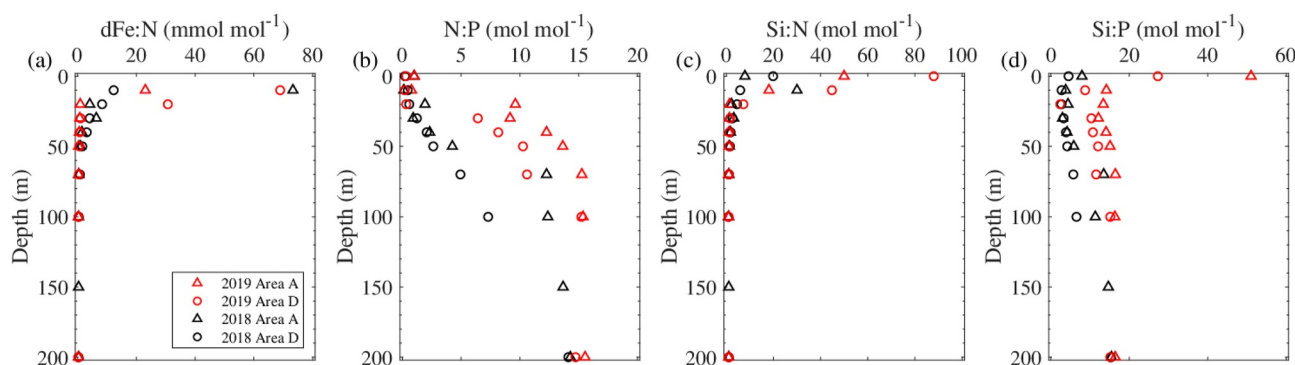


**Figure 9.** Comparisons of dFe and nutrient ratios in seawater obtained in 2018 and 2019.

implies that intense summer melting of glaciers has the potential to generate high-nutrient conditions in proglacial fjords and subsequently increase the production of diatoms during the summer.

We further expected that the production of large phytoplankton such as diatoms in 2019 would cause an increase of mesozooplankton populations. The food webs observed in 2019 were characterized by an abundance of heterotrophic nanoflagellates, unlike the observations in 2018 (Matsuno et al., 2020). Since the heterotrophic nanoflagellates are the essential link from bacteria to ciliates and heterotrophic dinoflagellates that are preyed upon by the mesozooplankton (Levinson & Nielsen, 2002), they would also contribute to an increase of biological production.

We note that the amount of light available for phytoplankton is also an important driver for making differences in summer production in Inglefield Bredning. Observations such as long-term monitoring of physical processes (e.g., glacier runoff and fjord circulation), biogeochemical conditions (nutrients, trace metals, organic carbon, and so on), and biological processes (e.g., primary production and zooplankton grazing) are also lacking in Inglefield Bredning. There is the limitation of our single “snapshot” observation, which was performed only in late summer. Future work is needed on relevant spatial and temporal scales to fully understand what are the drivers of the observed changes in biogeochemical conditions in Inglefield Bredning.

## 5. Summary

Our results indicate the impact of subglacial discharges from marine-terminating glaciers on the lower trophic levels of fjord ecosystems in Inglefield Bredning. The high abundance of phytoplankton, especially large diatoms, in the summer of 2019 was caused by the intensification of the upwelling plumes enriched with Fe, nitrate, phosphate, and silicate to the subsurface euphotic zone. Marine-terminating glaciers in Greenland are retreating and thinning (Howat & Eddy, 2011; Sakakibara & Sugiyama, 2018). Retreat of the glaciers above sea level may reduce summer productivity because pumping of nutrient-rich deep water by upwelling plumes will be lost, as suggested by recent studies (Hopwood et al., 2018; Meire et al., 2017). Moreover, high sediment surface plumes will reduce light availability for primary producers. Stronger and deeper stratification of fjords may also reduce summer productivity because nitrate supplied from upwelling plumes is blocked at the stratified layer. Further investigations will be required to elucidate the mechanism linking subglacial discharges and fjord productivity, and long-term monitoring will be required to evaluate changes to Greenlandic glaciers and coastal waters.

## Data Availability Statement

Copernicus Sentinel data (2018 and 2019) were processed with Sentinelflow (<https://github.com/juseg/sentinel-flow>) by J. Seguinot. Air temperature data are distributed by the U.S. National Oceanic and Atmospheric Administration National Climatic Data Center. BedMachine v4 (<https://doi.org/10.5067/VLJ5YXKCNGXO>) data were downloaded via the National Snow and Ice Data Center. Some of the CTD data in Inglefield Bredning were downloaded via the Oceans Melting Greenland website (<https://doi.org/10.5067/OMGEV-CTDS1>).

## Acknowledgments

We thank the members of the 2018 and 2019 field campaign in Greenland. Special thanks are due to T. Oshima, K. Peterson, I. Asaji, Y. Fujishi, and S. Daorana for providing logistical support. We are grateful to S. Matoba and I. Oyabu for assistance with sample handling and analysis and to K. Kondo for providing the glacier runoff data set. This research was funded by the Japanese Ministry of Education, Culture, Sports, Science and Technology through projects ArCS (JPMXD1300000000) and ArCS II (JPMXD1420318865). Funding was also provided by a Sasakawa Scientific Research Grant from The Japan Science Society. Data used in this study are available on Arctic Data archive System, <https://ads.nipr.ac.jp/dataset/A20181001-002> and <https://ads.nipr.ac.jp/dataset/A20191024-001>. Finally, we would like to thank two anonymous reviewers for their constructive comments.

## References

- Alkire, M. B., Falkner, K. K., Boyd, T., & Macdonald, R. W. (2010). Sea ice melt and meteoric water distributions in Nares Strait, Baffin Bay, and the Canadian Arctic Archipelago. *Journal of Marine Research*, 68(6), 767–798. <https://doi.org/10.1357/002224010796673867>
- Amon, R. M. W., & Budéus, G. (2003). Dissolved organic carbon distribution and origin in the Nordic Seas: Exchanges with the Arctic Ocean and the North Atlantic. *Journal of Geophysical Research*, 108(C7), 3221. <https://doi.org/10.1029/2002JC001594>
- Bâcle, J., Carmack, E. C., & Ingram, R. G. (2002). Water column structure and circulation under the North Water during spring transition: April–July 1998. *Deep-Sea Research Part II: Topical Studies in Oceanography*, 49(22), 4907–4925. [https://doi.org/10.1016/S0967-0645\(02\)00170-4](https://doi.org/10.1016/S0967-0645(02)00170-4)
- Batchelli, S., Muller, F. L., Chang, K., & Lee, C. (2010). Evidence for strong but dynamic iron–humic colloidal associations in humic-rich coastal waters. *Environmental Science & Technology*, 44(22), 8485–8490. <https://doi.org/10.1021/es101081c>
- Bendtsen, J., Rysgaard, S., Carlson, D. F., Meire, L., & Sejr, M. K. (2021). Vertical mixing in stratified fjords near tidewater outlet glaciers along Northwest Greenland. *Journal of Geophysical Research: Oceans*, 126(8), e2020JC016898. <https://doi.org/10.1029/2020JC016898>
- Benner, R., Louchouart, P., & Amon, R. M. W. (2005). Terrigenous dissolved organic matter in the Arctic Ocean and its transport to surface and deep waters of the North Atlantic. *Global Biogeochemical Cycles*, 19(2), GB2025. <https://doi.org/10.1029/2004GB002398>
- Bhatia, M. P., Das, S. B., Longnecker, K., Charette, M. A., & Kujawinski, E. B. (2010). Molecular characterization of dissolved organic matter associated with the Greenland ice sheet. *Geochimica et Cosmochimica Acta*, 74(13), 3768–3784. <https://doi.org/10.1016/j.gca.2010.03.035>
- Bhatia, M. P., Das, S. B., Xu, L., Charette, M. A., Wadham, J. L., & Kujawinski, E. B. (2013). Organic carbon export from the Greenland ice sheet. *Geochimica et Cosmochimica Acta*, 109, 329–344. <https://doi.org/10.1016/j.gca.2013.02.006>
- Bhatia, M. P., Kujawinski, E. B., Das, S. B., Breier, C. F., Henderson, P. B., & Charette, M. A. (2013). Greenland meltwater as a significant and potentially bioavailable source of iron to the ocean. *Nature Geoscience*, 6(4), 274–278. <https://doi.org/10.1038/ngeo1746>
- Bhatia, M. P., Waterman, P., Burgess, D. O., Williams, P. L., Bundy, R. M., Mellett, T., et al. (2021). Glaciers and Nutrients in the Canadian Arctic Archipelago marine system. *Global Biogeochemical Cycles*, 35(8), e2021GB006976. <https://doi.org/10.1029/2021gb006976>
- Birdwell, J. E., & Engel, A. S. (2010). Characterization of dissolved organic matter in cave and spring waters using UV–Vis absorbance and fluorescence spectroscopy. *Organic Geochemistry*, 41(3), 270–280. <https://doi.org/10.1016/j.orggeochem.2009.11.002>
- Björk, A. A., Kruse, J., & Michaelsen, P. B. (2015). Getting Greenland's glaciers right—A new data set of all official Greenlandic glacier names. *The Cryosphere*, 9(6), 2215–2218. <https://doi.org/10.5194/tc-9-2215-2015>
- Cao, F., Medeiros, P. M., & Miller, W. L. (2016). Optical characterization of dissolved organic matter in the Amazon River plume and the Adjacent Ocean: Examining the relative role of mixing, photochemistry, and microbial alterations. *Marine Chemistry*, 186, 178–188. <https://doi.org/10.1016/j.marchem.2016.09.007>
- Cape, M. R., Straneo, F., Beaird, N., Bundy, R. M., & Charette, M. A. (2019). Nutrient release to oceans from buoyancy-driven upwelling at Greenland tidewater glaciers. *Nature Geoscience*, 12(1), 34–39. <https://doi.org/10.1038/s41561-018-0268-4>
- Cape, M. R., Vernet, M., Pettit, E. C., Wellner, J., Truffer, M., Akie, G., et al. (2019). Circumpolar deep water impacts glacial meltwater export and coastal biogeochemical cycling along the West Antarctic Peninsula. *Frontiers in Marine Science*, 6, 144. <https://doi.org/10.3389/fmars.2019.00144>
- Carroll, D., Sutherland, D. A., Hudson, B., Moon, T., Catania, G. A., Shroyer, E. L., et al. (2016). The impact of glacier geometry on meltwater plume structure and submarine melt in Greenland fjords. *Geophysical Research Letters*, 43(18), 9739–9748. <https://doi.org/10.1002/2016gl070170>
- Coble, P. G. (1996). Characterization of marine and terrestrial DOM in seawater using excitation-emission matrix spectroscopy. *Marine Chemistry*, 51(4), 325–346. [https://doi.org/10.1016/0304-4203\(95\)00062-3](https://doi.org/10.1016/0304-4203(95)00062-3)
- Cory, R. M., & McKnight, D. M. (2005). Fluorescence spectroscopy reveals ubiquitous presence of oxidized and reduced quinones in dissolved organic matter. *Environmental Science & Technology*, 39(21), 8142–8149. <https://doi.org/10.1021/es0506962>
- Cowton, T. R., Sole, A. J., Nienow, P. W., Slater, D. A., & Christoffersen, P. (2018). Linear response of east Greenland's tidewater glaciers to ocean/atmosphere warming. *Proceedings of the National Academy of Sciences*, 115(31), 7907–7912. <https://doi.org/10.1073/pnas.1801769115>
- Cutter, G., Andersson, P., Codispoti, L., Croot, P., François, R., Lohan, M. C., et al. (2010). Sampling and sample-handling protocols for GEOTRACES cruises. Retrieved from <https://www.geotraces.org/methods-cookbook/>
- Evangelopoulos, A. (2002). Taxonomic notes on *Protoperdinium* (Peridinales, Dinophyceae) species in the Thermaikos Bay (North Aegean Sea, Greece). *Mediterranean Marine Science*, 3(2), 41–54. <https://doi.org/10.12681/mms.247>
- Evans, L. K., & Nishioka, J. (2018). Quantitative analysis of Fe, Mn and Cd from sea ice and seawater in the Chukchi Sea, Arctic Ocean. *Polar Science*, 17, 50–58. <https://doi.org/10.1016/j.polar.2018.07.002>
- Forsch, K. O., Hahn-Woernle, L., Sherrell, R. M., Rocanova, V. J., Bu, K., Burdige, D., et al. (2021). Seasonal dispersal of fjord meltwaters as an important source of iron and manganese to coastal Antarctic phytoplankton. *Biogeosciences*, 18(23), 6349–6375. <https://doi.org/10.5194/bg-18-6349-2021>
- Fried, M. J., Catania, G. A., Bartholomaeus, T. C., Duncan, D., Davis, M., Stearns, L. A., et al. (2015). Distributed subglacial discharge drives significant submarine melt at a Greenland tidewater glacier. *Geophysical Research Letters*, 42(21), 9328–9336. <https://doi.org/10.1002/2015gl065806>
- Fukuyo, Y., Inoue, H., & Takayama, H. (1997). Class Dinophyceae. In M. Chihara & M. Murano (Eds.), *An illustrated guide to marine plankton in Japan* (pp. 31–112). Tokai University Press.
- Gade, H. G. (1979). Melting of ice in sea water: A primitive model with application to the Antarctic ice shelf and icebergs. *Journal of Physical Oceanography*, 9(1), 189–198. [https://doi.org/10.1175/1520-0485\(1979\)009<0189:moisw>2.0.co;2](https://doi.org/10.1175/1520-0485(1979)009<0189:moisw>2.0.co;2)
- Gardner, A. S., Moholdt, G., Graham Cogley, J., Wouters, B., Arendt, A. A., Wahr, J., et al. (2013). A reconciled estimate of glacier contributions to sea level rise: 2003 to 2009. *Science*, 340(6134), 852–857. <https://doi.org/10.1126/science.1234532>
- Gledhill, M., & Buck, K. N. (2012). The organic complexation of iron in the marine environment: A review. *Frontiers in Microbiology*, 3, 69. <https://doi.org/10.3389/fmicb.2012.00069>
- Hasle, G. R., & Syvertsen, E. E. (1997). Marine diatoms. In C. R. Tomas (Ed.), *Identifying marine phytoplankton* (pp. 5–385). Academic Press.
- Hawkins, J. R., Benning, L. G., Raiswell, R., Kaulich, B., Araki, T., Abyaneh, M., et al. (2018). Biolabile ferrous iron bearing nanoparticles in glacial sediments. *Earth and Planetary Science Letters*, 493, 92–101. <https://doi.org/10.1016/j.epsl.2018.04.022>
- Hawkins, J. R., Wadham, J. L., Benning, L. G., Hendry, K. R., Tranter, M., Tedstone, A., et al. (2017). Ice sheets as a missing source of silica to the polar oceans. *Nature Communications*, 8(1), 1–10. <https://doi.org/10.1038/ncomms14198>
- Hawkins, J. R., Wadham, J. L., Tranter, M., Raiswell, R., Benning, L. G., Statham, P. J., et al. (2014). Ice sheets as a significant source of highly reactive nanoparticulate iron to the oceans. *Nature Communications*, 5(1), 3929. <https://doi.org/10.1038/ncomms4929>
- Ho, T.-Y., Quigg, A., Finkel, Z. V., Milligan, A. J., Wyman, K., Falkowski, P. G., & Morel, F. M. M. (2003). The elemental composition of some marine phytoplankton. *Journal of Phycology*, 39(6), 1145–1159. <https://doi.org/10.1111/j.0022-3646.2003.03-090.x>
- Holland, A. T., Williamson, C. J., Sgouridis, F., Tedstone, A. J., McCutcheon, J., Cook, J. M., et al. (2019). Dissolved organic nutrients dominate melting surface ice of the Dark Zone (Greenland Ice Sheet). *Biogeosciences*, 16(16), 3283–3296. <https://doi.org/10.5194/bg-16-3283-2019>

- Hopwood, M. J., Carroll, D., Browning, T. J., Meire, L., Mortensen, J., Krisch, S., & Achterberg, E. P. (2018). Non-linear response of summer-time marine productivity to increased meltwater discharge around Greenland. *Nature Communications*, 9(1), 3256. <https://doi.org/10.1038/s41467-018-05488-8>
- Hopwood, M. J., Carroll, D., Dunse, T., Hodson, A., Holding, J. M., Iriarte, J. L., et al. (2020). Review article: How does glacier discharge affect marine biogeochemistry and primary production in the Arctic? *The Cryosphere*, 14(4), 1347–1383. <https://doi.org/10.5194/tc-14-1347-2020>
- Hopwood, M. J., Connelly, D. P., Arendt, K. E., Juul-Pedersen, T., Stinchcombe, M. C., Meire, L., et al. (2016). Seasonal changes in Fe along a glaciated Greenlandic fjord. *Frontiers in Earth Science*, 4. <https://doi.org/10.3389/feart.2016.00015>
- Howat, I. M., & Eddy, A. (2011). Multi-decadal retreat of Greenland's marine-terminating glaciers. *Journal of Glaciology*, 57(203), 389–396. <https://doi.org/10.3189/002214311796905631>
- Huguet, A., Vacher, L., Relexans, S., Saubusse, S., Froidefond, J. M., & Parlanti, E. (2009). Properties of fluorescent dissolved organic matter in the Gironde Estuary. *Organic Geochemistry*, 40(6), 706–719. <https://doi.org/10.1016/j.orggeochem.2009.03.002>
- Jørgensen, L., Stedmon, C. A., Kragh, T., Markager, S., Middelboe, M., & Søndergaard, M. (2011). Global trends in the fluorescence characteristics and distribution of marine dissolved organic matter. *Marine Chemistry*, 126(1–4), 139–148. <https://doi.org/10.1016/j.marchem.2011.05.002>
- Kanna, N., Sugiyama, S., Fukamachi, Y., Nomura, D., & Nishioka, J. (2020). Iron supply by subglacial discharge into a fjord near the front of a marine-terminating glacier in northwestern Greenland. *Global Biogeochemical Cycles*, 34(10), e2020GB006567. <https://doi.org/10.1029/2020gb006567>
- Kanna, N., Sugiyama, S., Ohashi, Y., Sakakibara, D., Fukamachi, Y., & Nomura, D. (2018). Upwelling of macronutrients and dissolved inorganic carbon by a subglacial freshwater driven plume in Bowdoin Fjord, northwestern Greenland. *Journal of Geophysical Research: Biogeosciences*, 123(5), 1666–1682. <https://doi.org/10.1029/2017jg004248>
- Kellerman, A. M., Hawkings, J. R., Wadham, J. L., Kohler, T. J., Stibal, M., Grater, E., et al. (2020). Glacier outflow dissolved organic matter as a window into seasonally changing carbon sources: Leverett Glacier, Greenland. *Journal of Geophysical Research: Biogeosciences*, 125(4), e2019JG005161. <https://doi.org/10.1029/2019jg005161>
- Kondo, K., Sugiyama, S., Sakakibara, D., & Fukumoto, S. (2021). Flood events caused by discharge from Qaanaaq Glacier, northwestern Greenland. *Journal of Glaciology*, 67(263), 500–510. <https://doi.org/10.1017/jog.2021.3>
- Krause, J., Hopwood, M. J., Höfer, J., Krisch, S., Achterberg, E. P., Alarcón, E., et al. (2021). Trace element (Fe, Co, Ni and Cu) dynamics across the salinity gradient in Arctic and Antarctic glacier fjords. *Frontiers in Earth Science*, 9. <https://doi.org/10.3389/feart.2021.725279>
- Kudo, I. (2003). Change in the uptake and cellular Si:N ratio in diatoms responding to the ambient Si:N ratio and growth phase. *Marine Biology*, 143(1), 39–46. <https://doi.org/10.1007/s00227-003-1063-2>
- Laglera, L. M., Sukekava, C., Slagter, H. A., Downes, J., Aparicio-Gonzalez, A., & Gerringa, L. J. (2019). First quantification of the controlling role of humic substances in the transport of iron across the surface of the Arctic Ocean. *Environmental Science & Technology*, 53(22), 13136–13145. <https://doi.org/10.1021/acs.est.9b04240>
- Laglera, L. M., & van den Berg, C. M. G. (2009). Evidence for geochemical control of iron by humic substances in seawater. *Limnology & Oceanography*, 54(2), 610–619. <https://doi.org/10.4319/lo.2009.54.2.0610>
- Laufer-Meisner, K., Michaud, A. B., Maisch, M., Byrne, J. M., Kappler, A., Patterson, M. O., et al. (2021). Potentially bioavailable iron produced through benthic cycling in glaciated Arctic fjords of Svalbard. *Nature Communications*, 12(1), 1–13. <https://doi.org/10.1038/s41467-021-21558-w>
- Lawson, E. C., Wadham, J. L., Tranter, M., Stibal, M., Lis, G. P., Butler, C. E. H., et al. (2014). Greenland Ice Sheet exports labile organic carbon to the Arctic oceans. *Biogeosciences*, 11(14), 4015–4028. <https://doi.org/10.5194/bg-11-4015-2014>
- Levinson, H., & Nielsen, T. G. (2002). The trophic role of marine pelagic ciliates and heterotrophic dinoflagellates in arctic and temperate coastal ecosystems: A cross-latitude comparison. *Limnology & Oceanography*, 47(2), 427–439. <https://doi.org/10.4319/lo.2002.47.2.0427>
- Lydersen, C., Assmy, P., Falk-Petersen, S., Kohler, J., Kovacs, K. M., Reigstad, M., et al. (2014). The importance of tidewater glaciers for marine mammals and seabirds in Svalbard, Norway. *Journal of Marine Systems*, 129, 452–471. <https://doi.org/10.1016/j.jmarsys.2013.09.006>
- Macdonald, R. W., McLaughlin, F. A., & Wong, C. S. (1986). The storage of reactive silicate samples by freezing. *Limnology & Oceanography*, 31, 1139–1142. <https://doi.org/10.4319/lo.1986.31.5.1139>
- Maeda, M. (1997). Suborder oligotrichida. In M. Chihara & M. Murano (Eds.), *An illustrated guide to marine plankton in Japan* (pp. 397–420). Tokai University Press.
- Maldonado, M. T., & Price, N. M. (1996). Influence of N substrate on Fe requirements of marine centric diatoms. *Marine Ecology Progress Series*, 141, 161–172. <https://doi.org/10.3354/meps141161>
- Mankoff, K. D., Noël, B., Fettweis, X., Ahlström, A. P., Colgan, W., Kondo, K., et al. (2020). Greenland liquid water discharge from 1958 through 2019. *Earth System Science Data*, 12(4), 2811–2841. <https://doi.org/10.5194/essd-12-2811-2020>
- Mankoff, K. D., Straneo, F., Cenedese, C., Das, S. B., Richards, C. G., & Singh, H. (2016). Structure and dynamics of a subglacial discharge plume in a Greenlandic fjord. *Journal of Geophysical Research: Oceans*, 121(12), 8670–8688. <https://doi.org/10.1002/2016JC011764>
- Marshall, M. G., Kellerman, A. M., Wadham, J. L., Hawkings, J. R., Daneri, G., Torres, R., et al. (2021). Seasonal changes in dissolved organic matter composition in a Patagonian fjord affected by glacier melt inputs. *Frontiers in Marine Science*, 8, 276. <https://doi.org/10.3389/fmars.2021.612386>
- Matsuno, K., Kanna, N., Sugiyama, S., Yamaguchi, A., & Yang, E. (2020). Impacts of meltwater discharge from marine-terminating glaciers on the protist community in Inglefield Bredning, northwestern Greenland. *Marine Ecology. Progress Series*, 642, 55–65. <https://doi.org/10.3354/meps13324>
- Meire, L., Meire, P., Struyf, E., Krawczyk, D. W., Arendt, K. E., Yde, J. C., et al. (2016). High export of dissolved silica from the Greenland Ice Sheet. *Geophysical Research Letters*, 43(17), 9173–9182. <https://doi.org/10.1002/2016GL070191>
- Meire, L., Mortensen, J., Meire, P., Juul-Pedersen, T., Sejr, M. K., Rysgaard, S., et al. (2017). Marine-terminating glaciers sustain high productivity in Greenland fjords. *Global Change Biology*, 23(12), 5344–5357. <https://doi.org/10.1111/gcb.13801>
- Menden-Deuer, S., & Lessard, E. J. (2000). Carbon to volume relationships for dinoflagellates, diatoms, and other protist plankton. *Limnology & Oceanography*, 45(3), 569–579. <https://doi.org/10.4319/lo.2000.45.3.0569>
- Morel, F. M. M., & Price, N. M. (2003). The biogeochemical cycles of trace metals in the oceans. *Science*, 300(5621), 944–947. <https://doi.org/10.1126/science.1083545>
- Morlighem, M., Williams, C. N., Rignot, E., An, L., Arndt, J. E., Bamber, J. L., et al. (2017). BedMachine v3: Complete bed topography and ocean bathymetry mapping of Greenland from multibeam echo sounding combined with mass conservation. *Geophysical Research Letters*, 44(21), 11051–11061. <https://doi.org/10.1002/2017GL074954>
- Mortensen, J., Bendtsen, J., Motyka, R. J., Lennert, K., Truffer, M., Fahnestock, M., & Rysgaard, S. (2013). On the seasonal freshwater stratification in the proximity of fast-flowing tidewater outlet glaciers in a sub-Arctic sill fjord. *Journal of Geophysical Research: Oceans*, 118(3), 1382–1395. <https://doi.org/10.1002/jgrc.20134>

- Naito, A., Abe, Y., Matsuno, K., Nishizawa, B., Kanna, N., Sugiyama, S., & Yamaguchi, A. (2019). Surface zooplankton size and taxonomic composition in Bowdoin Fjord, north-western Greenland: A comparison of ZooScan, OPC and microscopic analyses. *Polar Science*, 19, 120–129. <https://doi.org/10.1016/j.polar.2019.01.001>
- Nishioka, J., & Obata, H. (2017). Dissolved iron distribution in the western and central subarctic Pacific. *Limnology & Oceanography*, 62(5), 2004–2022. <https://doi.org/10.1002/lno.10548>
- Nishizawa, B., Kanna, N., Ohashi, Y., Sakakibara, D., Asaji, I., Abe, Y., et al. (2019). Contrasting assemblages of seabirds in the subglacial meltwater plume and oceanic water of Bowdoin Fjord, northwestern Greenland. *ICES Journal of Marine Science*, 77(2), 711–720. <https://doi.org/10.1093/icesjms/fsz213>
- Ohashi, Y., Aoki, S., Matsumura, Y., Sugiyama, S., Kanna, N., & Sakakibara, D. (2020). Vertical distribution of water mass properties under the influence of subglacial discharge in Bowdoin Fjord, northwestern Greenland. *Ocean Science*, 16(3), 545–564. <https://doi.org/10.5194/os-16-545-2020>
- Opsahl, S., Benner, R., & Amon, R. M. W. (1999). Major flux of terrigenous dissolved organic matter through the Arctic Ocean. *Limnology & Oceanography*, 44(8), 2017–2023. <https://doi.org/10.4319/lno.1999.44.8.2017>
- Osborn, T. R. (1980). Estimates of the local rate of vertical diffusion from dissipation measurements. *Journal of Physical Oceanography*, 10(1), 83–89. [https://doi.org/10.1175/1520-0485\(1980\)010<0083:eotro>2.0.co;2](https://doi.org/10.1175/1520-0485(1980)010<0083:eotro>2.0.co;2)
- Pain, A. J., Martin, J. B., Martin, E. E., Rahman, S., & Ackermann, P. (2020). Differences in the quantity and quality of organic matter exported from Greenlandic glacial and deglaciated watersheds. *Global Biogeochemical Cycles*, 34(10), e2020GB006614. <https://doi.org/10.1029/2020gb006614>
- Paulsen, M. L., Müller, O., Larsen, A., Möller, E. F., Middelboe, M., Sej, M. K., & Stedmon, C. (2019). Biological transformation of Arctic dissolved organic matter in a NE Greenland fjord. *Limnology & Oceanography*, 64(3), 1014–1033. <https://doi.org/10.1002/lno.11091>
- Paulsen, M. L., Nielsen, S. E., Müller, O., Möller, E. F., Stedmon, C. A., Juul-Pedersen, T., et al. (2017). Carbon bioavailability in a high Arctic fjord influenced by glacial meltwater, NE Greenland. *Frontiers in Marine Science*, 4, 176. <https://doi.org/10.3389/fmars.2017.00176>
- Podolskiy, E. A., & Sugiyama, S. (2020). Soundscape of a narwhal summering ground in a glacier fjord (Inglefield Bredning, Greenland). *Journal of Geophysical Research: Oceans*, 125(5), e2020JC016116. <https://doi.org/10.1029/2020jc016116>
- Porter, D. F., Tinto, K. J., Boghosian, A., Cochran, J. R., Bell, R. E., Manizade, S. S., & Sonntag, J. G. (2014). Bathymetric control of tidewater glacier mass loss in northwest Greenland. *Earth and Planetary Science Letters*, 401, 40–46. <https://doi.org/10.1016/j.epsl.2014.05.058>
- Price, N. M. (2005). The elemental stoichiometry and composition of an iron-limited diatom. *Limnology & Oceanography*, 50(4), 1159–1171. <https://doi.org/10.4319/lno.2005.50.4.1159>
- Rignot, E., Koppes, M., & Velicogna, I. (2010). Rapid submarine melting of the calving faces of West Greenland glaciers. *Nature Geoscience*, 3(3), 187–191. <https://doi.org/10.1038/ngeo765>
- Rysgaard, S., Boone, W., Carlson, D., Sej, M. K., Bendtsen, J., Juul-pedersen, T., et al. (2020). An updated view on water masses on the pan-west Greenland continental shelf and their link to proglacial fjords. *Journal of Geophysical Research: Oceans*, 125(2). <https://doi.org/10.1029/2019jc015564>
- Sakakibara, D., & Sugiyama, S. (2018). Ice front and flow speed variations of marine-terminating outlet glaciers along the coast of Prudhoe Land, northwestern Greenland. *Journal of Glaciology*, 64(244), 300–310. <https://doi.org/10.1017/jog.2018.20>
- Sarthou, G., Timmermans, K. R., Blain, S., & Tréguer, P. (2005). Growth physiology and fate of diatoms in the ocean: A review. *Journal of Sea Research*, 53(1), 25–42. <https://doi.org/10.1016/j.seares.2004.01.007>
- Sasgen, I., Wouters, B., Gardner, A. S., King, M. D., Tedesco, M., Landerer, F. W., et al. (2020). Return to rapid ice loss in Greenland and record loss in 2019 detected by the GRACE-FO satellites. *Communications Earth & Environment*, 1(1), 8. <https://doi.org/10.1038/s43247-020-0010-1>
- Schroth, A. W., Crusius, J., Hoyer, I., & Campbell, R. (2014). Estuarine removal of glacial iron and implications for iron fluxes to the ocean. *Geophysical Research Letters*, 41(11), 3951–3958. <https://doi.org/10.1002/2014gl060199>
- Sherr, B. F., & Sherr, E. B. (1983). Enumeration of heterotrophic microprotozoa by epifluorescence microscopy. *Estuarine, Coastal and Shelf Science*, 16, 1–7. [https://doi.org/10.1016/0272-7714\(83\)90089-6](https://doi.org/10.1016/0272-7714(83)90089-6)
- Sohrin, Y., Urushihara, S., Nakatsuka, S., Kono, T., Higo, E., Minami, T., et al. (2008). Multielemental determination of GEOTRACES key trace metals in seawater by ICPMS after preconcentration using an ethylenediaminetriacetic acid chelating resin. *Analytical Chemistry*, 80(16), 6267–6273. <https://doi.org/10.1021/ac800500f>
- Straneo, F., & Heimbach, P. (2013). North Atlantic warming and the retreat of Greenland's outlet glaciers. *Nature*, 504(7478), 36–43. <https://doi.org/10.1038/nature12854>
- Straneo, F., Sutherland, D. A., Holland, D., Gladish, C., Hamilton, G. S., Johnson, H. L., et al. (2012). Characteristics of ocean waters reaching Greenland's glaciers. *Annals of Glaciology*, 53(60), 202–210. <https://doi.org/10.3189/2012AoG60A059>
- Sugiyama, S., Kanna, N., Sakakibara, D., Ando, T., Asaji, I., Kondo, K., et al. (2021). Rapidly changing glaciers, ocean and coastal environments, and their impact on human society in the Qaanaaq region, northwestern Greenland. *Polar Science*, 27, 100632. <https://doi.org/10.1016/j.polar.2020.100632>
- Sun, J., & Liu, D. (2003). Geometric models for calculating cell biovolume and surface area for phytoplankton. *Journal of Plankton Research*, 25(11), 1331–1346. <https://doi.org/10.1093/plankt/fbg096>
- Sunda, W., & Huntsman, S. (1997). Interrelated influence of iron, light and cell size on marine phytoplankton growth. *Nature*, 390(6658), 389–392. <https://doi.org/10.1038/37093>
- Sunda, W. G., & Huntsman, S. A. (1995). Iron uptake and growth limitation in oceanic and coastal phytoplankton. *Marine Chemistry*, 50(1–4), 189–206. [https://doi.org/10.1016/0304-4203\(95\)00035-p](https://doi.org/10.1016/0304-4203(95)00035-p)
- Sutherland, D. A., Jackson, R. H., Kienholz, C., Amundson, J. M., Dryer, W. P., Duncan, D., et al. (2019). Direct observations of submarine melt and subsurface geometry at a tidewater glacier. *Science*, 365(6451), 369–374. <https://doi.org/10.1126/science.aax3528>
- Suzuki, R., & Ishimaru, T. (1990). An improved method for the determination of phytoplankton chlorophyll using N, N-dimethylformamide. *Journal of Oceanography*, 46(4), 190–194. <https://doi.org/10.1007/bf02125580>
- Takeda, S. (1998). Influence of iron availability on nutrient consumption ratio of diatoms in oceanic waters. *Nature*, 393(6687), 774–777. <https://doi.org/10.1038/31674>
- Tanaka, K., Kuma, K., Hamasaki, K., & Yamashita, Y. (2014). Accumulation of humic-like fluorescent dissolved organic matter in the Japan Sea. *Scientific Reports*, 4(1), 5292. <https://doi.org/10.1038/srep05292>
- Taniguchi, A. (1997). Suborder Tintinnina. In M. Chihara & M. Murano (Eds.), *An illustrated guide to marine plankton in Japan* (pp. 421–483). Tokai University Press.
- Tedesco, M., & Fettweis, X. (2020). Unprecedented atmospheric conditions (1948–2019) drive the 2019 exceptional melting season over the Greenland ice sheet. *The Cryosphere*, 14(4), 1209–1223. <https://doi.org/10.5194/tc-14-1209-2020>



- Timmermans, K. R., Van Der Wagt, B., & De Baar, H. J. (2004). Growth rates, half-saturation constants, and silicate, nitrate, and phosphate depletion in relation to iron availability of four large, open-ocean diatoms from the Southern Ocean. *Limnology & Oceanography*, 49(6), 2141–2151. <https://doi.org/10.4319/lo.2004.49.6.2141>
- Trusel, L. D., Das, S. B., Osman, M. B., Evans, M. J., Smith, B. E., Fettweis, X., et al. (2018). Nonlinear rise in Greenland runoff in response to post-industrial Arctic warming. *Nature*, 564(7734), 104–108. <https://doi.org/10.1038/s41586-018-0752-4>
- Twining, B. S., & Baines, S. B. (2013). The trace metal composition of marine phytoplankton. *Annual Review of Marine Science*, 5(1), 191–215. <https://doi.org/10.1146/annurev-marine-121211-172322>
- Twining, B. S., Baines, S. B., Fisher, N. S., & Landry, M. R. (2004). Cellular iron contents of plankton during the Southern Ocean Iron Experiment (SOFEX). *Deep Sea-Research Part I*, 51(12), 1827–1850. <https://doi.org/10.1016/j.dsr.2004.08.007>
- Walker, S. A., Amon, R. M., Stedmon, C., Duan, S., & Louchouart, P. (2009). The use of PARAFAC modeling to trace terrestrial dissolved organic matter and fingerprint water masses in coastal Canadian Arctic surface waters. *Journal of Geophysical Research*, 114(G4), G00F06. <https://doi.org/10.1029/2009jg000990>
- Wang, Y., Sugiyama, S., & Bjørk, A. A. (2021). Surface elevation change of glaciers along the coast of Prudhoe land, northwestern Greenland from 1985 to 2018. *Journal of Geophysical Research: Earth Surface*, 126(11), e2020JF006038. <https://doi.org/10.1029/2020jg006038>
- Welschmeyer, N. A. (1994). Fluorometric analysis of chlorophyll a in the presence chlorophyll b and phaeopigments. *Limnology & Oceanography*, 39(8), 1985–1992. <https://doi.org/10.4319/lo.1994.39.8.1985>
- Williams, P. L., Burgess, D. O., Waterman, S., Roberts, M., Bertrand, E. M., & Bhatia, M. P. (2021). Nutrient and carbon export from a tidewater glacier to the coastal ocean in the Canadian Arctic Archipelago. *Journal of Geophysical Research: Biogeosciences*, 126(9), e2021JG006289. <https://doi.org/10.1029/2021jg006289>
- Willis, J. K., Carroll, D., Fenty, I., Kohli, G., Khazendar, A., Rutherford, M., et al. (2018). Ocean-ice interactions in Inglefield Gulf: Early results from NASA's Oceans Melting Greenland mission. *Oceanography*, 31(2), 100–108. <https://doi.org/10.5670/oceanog.2018.211>
- Yamashita, Y., Nishioka, J., Obata, H., & Ogawa, H. (2020). Shelf humic substances as carriers for basin-scale iron transport in the North Pacific. *Scientific Report*, 10(1), 4505. <https://doi.org/10.1038/s41598-020-61375-7>
- Yamashita, Y., Panton, A., Mahaffey, C., & Jaffe, R. (2011). Assessing the spatial and temporal variability of dissolved organic matter in Liverpool Bay using excitation–emission matrix fluorescence and parallel factor analysis. *Ocean Dynamics*, 61(5), 569–579. <https://doi.org/10.1007/s10236-010-0365-4>
- Yamashita, Y., Tsukasaki, A., Nishida, T., & Tanoue, E. (2007). Vertical and horizontal distribution of fluorescent dissolved organic matter in the Southern Ocean. *Marine Chemistry*, 106(3), 498–509. <https://doi.org/10.1016/j.marchem.2007.05.004>
- Zhang, J.-Z., & Ortner, P. B. (1998). Effect of thawing condition on the recovery of reactive silicic acid from frozen natural water samples. *Water Research*, 32(8), 2553–2555. [https://doi.org/10.1016/s0043-1354\(98\)00005-0](https://doi.org/10.1016/s0043-1354(98)00005-0)
- Zhang, R., John, S. G., Zhang, J., Ren, J., Wu, Y., Zhu, Z., et al. (2015). Transport and reaction of iron and iron stable isotopes in glacial meltwaters on Svalbard near Kongsfjorden: From rivers to estuary to ocean. *Earth and Planetary Science Letters*, 424, 201–211. <https://doi.org/10.1016/j.epsl.2015.05.031>